2015

Modeling fan broadband noise from jet engines and rod-airfoil benchmark case for broadband noise prediction

Bharat Raj Agrawal
Iowa State University

Modeling fan broadband noise from jet engines and rod-airfoil benchmark case for broadband noise prediction

by

Bharat Raj Agrawal

A thesis submitted to the graduate faculty

in partial fulfillment of the requirements for the degree of

MASTER OF SCIENCE

Major: Aerospace Engineering

Program of Study Committee:

Anupam Sharma, Major Professor

Alric Rothmayer

Alberto Passalacqua

Iowa State University

Ames, Iowa

2015

DEDICATION

I would like to dedicate this thesis to my parents.

TABLE OF CONTENTS

LIST OF FIGURES

ABSTRACT

This work has two primary parts: (1) an exhaustive literature review highlighting the need and the direction to study broadband noise generation from the fan stage of a modern high bypass ratio turbofan engine, and (2) a benchmark study of noise generation by the flow over a rod and an airfoil in tandem arrangement. The literature review highlights that not all the experimental data has been consistently explained with the theory and thus these gaps are required to be filled in to improve the fan noise prediction during the design phases. The benchmark case provides flow conditions where the upstream located circular rod sheds periodic vortices and creates turbulence which interacts with downstream located symmetric airfoil at zero angle of attack. This interaction produces noise which radiates to farfield. The periodic shedding and the resulting turbulence provides energy to the tonal and broadband components of the total noise. This test case is used to validate a new approach to predict noise in farfield which uses incompressible flow solver, pimpleFoam (part of OpenFOAM), along with Amiet's theory.

CHAPTER 1. GENERAL INTRODUCTION

The National Aeronautics and Space Administration (NASA) agency predicts doubling of commercial air traffic over next two decades and aircraft noise is seen as a significant factor becoming increasingly prominent and negatively impacting the growth of civil aviation. NASA has thus prescribed noise reduction targets for aircraft designers to achieve in order to sustain the required growth of commercial traffic. The policies on allowable noise by commercial aircraft are regulated by Federal Aviation Administration (FAA), these policies specify upper limits on the total noise perceived at certain locations due to an aircraft at take-off and landing conditions. For typical modern passenger airplanes, the total noise under test conditions are dominated by noise produced by the fan of the engine and its jet. Since introduction, the turbofan engines have undergone a continuous increase in bypass ratio which is set to continue to increase further. An increase in bypass ratio reduces the gradients in jet shear layer which reduces jet noise production. However, increasing the bypass ratio implies increasing the fan diameter, this causes the fan noise to increase.

The second chapter of this work presents detailed literature review of analytical and computational work relevant to fan noise. The first part of the review focuses on highlighting the need to study fan noise, different noise production mechanisms in an engine fan stage, and presents a few critical results from two major experimental campaigns [3, 4] designed to study fan noise. These experiments classified and quantified different noise generation mechanisms and broadly grouped them as interaction and self noise sources. Scaling analyses using data from these experiments are presented that question generally accepted noise scaling rules of thumb. The second part of the review focuses on fundamental physics behind aerodynamic noise production in general, noise production mechanisms for the interaction and self noise sources and transmission and radiation of acoustic energy into farfield. The Boeing experiments [3]

demonstrated that "rotor-stator interaction noise" is the most dominant noise source. There, a general semi-analytical method to predict this noise source is also presented.

Interaction and self noise are different from jet noise in nature because the former are sourced at turbulent structures causing unsteady pressures on solid surfaces, whereas jet noise is caused due to shear in the bulk of the turbulence. Interaction noise is differentiated from self noise on the basis of the source of turbulence, which for self noise is generated at the same surface where noise is produced whereas for interaction noise the turbulence is generated by a surface upstream of the one producing the noise.

The third chapter focuses on a model problem for interaction noise. In this model problem, an upstream located two-dimensional circular cylinder sheds vortices at periodic intervals, these vortices convects downstream and breaks down to smaller scales of turbulence, thereby giving a broad spectrum of turbulence scales. This turbulent flow then impinges on a NACA 0012 airfoil located downstream at zero angle of attack. Large Eddy Simulations (LES) were carried out with incompressible and compressible flow solvers and time history of specific fluid data is extracted for aeroacoustic analysis. The incompressible and compressible flow simulation data are used with Amiet's theory and Ffowcs Williams-Hawkings (FW-H) acoustic analogy to predict farfield sound. The flow and acoustic predictions are compared with experimental data available from literature. The flowfield and the farfield noise spectra matches well with the literature.

CHAPTER 2. REVIEW OF LITERATURE

The demand for air travel has been continuously increasing and the aviation industry is projected to continue to grow in the next few decades. The National Aeronautics and Space Administration (NASA) agency predicts doubling of commercial air traffic over next two decades. One of the issues that the community needs to address to continue this growth is the adverse impact of noise emitted by these aircraft. Aircraft noise adversely affects both the community living around airports (*community* noise) as well as passengers and crew (*cabin* noise). Community noise, for subsonic flights, is a problem primarily during take-off and approach. Supersonic cruisers can radiate sonic boom to the ground from their cruise altitude! Cabin noise can be discomforting through the entire flight duration, however specific cabin noise sources are prominent only during specific phases of flight. The problems mentioned above are related to civil transport. Noise radiation caused by military transport can pose significant health risks. Military personnel who work on aircraft carriers are exposed to sustained elevated noise levels, which lead to hearing losses and other health hazards. The economic implications of the problem are severe - e.g., the U.S. Department of Veterans Affairs spends over $1 billion per year for hearing loss.

Efforts towards controlling and mitigating aircraft noise have been ongoing for over four decades. The Federal Aviation Administration (FAA) regulates the maximum allowable noise level for each flight based on the maximum take-off weight, time of day, etc. Such regulations have certainly helped in controlling the noise exposure. These regulations are becoming increasingly stringent as the number of flights is continually increasing. NASA has formulated an aggressive set of noise reduction goals for the next three generations of aircraft. These generations, designated by "N+1", "N+2" and "N+3", are expected to reduce noise by 32 dB, 42 dB and 71 dB by 2015, 2020 and 2025 respectively [8]. These noise reduction goals are with

reference to the baseline determined by the current generation of aircraft. Similarly, NASA has also set goals for reducing NOx and CO2 emissions, and specific fuel consumption.

The scale of improvements desired by NASA has prompted accelerated research into noise reduction technologies. The research carried out towards "N+1" shows that existing aircraft could achieve the goal by employing existing noise-reduction technology. However, significant research investment is necessary to achieve the "N+2" and "N+3" goals. It is understood that such large noise reduction will require a back-to-the-drawing-board approach, wherein a complete redesign of aircraft is likely. While a systems approach is necessary, contributions towards overall noise reduction have to come from powerplants (engines) and airframe (including landing gear). Careful system-wide as well as component-wide research activities are therefore required.

Aircraft Noise Sources

There are multiple sources of noise generation in an aircraft. During different phases of a flight, the contribution to overall noise by different sources is different. In the beginning of the jet age, noise from the jet exhaust overwhelmed any other noise source. Modern, large civil transport aircraft are powered by high-bypass turbofan engines primarily because of their relatively low thrust specific fuel consumption. These engines impart a small momentum change to a large amount of air (which bypasses the core), thereby minimizing the loss of kinetic energy in exhaust flow. A by-product of reduced exhaust velocity is reduction of jet noise, which scales approximately to eighth power of exhaust flow Mach number. There have been other technological advances as well such as chevron nozzles [9] that have further reduced jet noise. Other noise sources from engines and airframe have therefore now become very important.

Figure 2.1 show the overall as well as component noise levels for a typical civil transport aircraft. The noise levels are shown separately at approach and takeoff flight conditions. Noise from fan has been split into two – inlet radiated and exhaust (aft) radiated. Figure 2.1 show that inlet radiated fan noise dominates during approach, while both exhaust radiated fan noise and jet noise dominate during takeoff. When comparing relative noise magnitudes it should be borne in mind that sound pressure (also energy energy) is measured in decibels (or dB), which

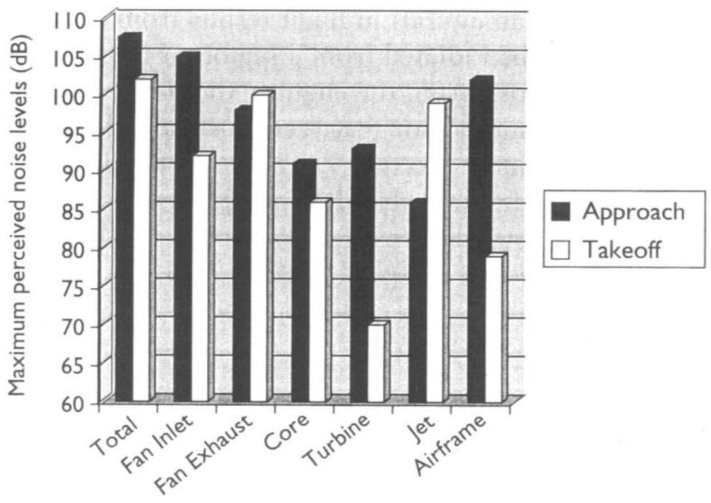

Figure 2.1: Source breakdown of perceived noise (reproduced from Owens [1]).

is a logarithmic unit. The overall noise level in dB is therefore not linear but logarithmic sum of component noise levels.

Fan Noise

Fan noise has been studied in great detail over the past few decades. Based on its frequency spectrum characteristics, fan noise is classified into two categories: tonal and broadband. Figure 2.2 shows the measured far field sound pressure level spectra from a modern turbofan engine at two rotational speeds. In this spectral plot, frequency is normalized by the shaft rotation frequency. This non-dimensional frequency (referred to as engine order, EO) is independent of the shaft rotation rate and hence permits comparison of spectra at different speeds. The fundamental blade passing frequency (BPF) in this non-dimensional representation is equal to the number of blades regardless of the shaft speed. A similar scaling, normalizing frequency with BPF, is also used to clearly identify BPF and its harmonics. At subsonic rotor tip speeds, the spectrum is predominantly broadband with relatively few sharp peaks. The peaks, signifying tonal noise, correspond to rotor blade passing frequency (BPF) and its harmonics. The noise generation mechanism for these tones is now understood to be the interaction of mean rotor viscous wake interaction with downstream stators [10]. At supersonic rotor tip speeds, the spectrum displays many more tones (at engine orders not just blade passing orders). These

arise because of the formation of shock waves at the leading edge of rotor blades. Blade non-uniformities (especially stagger variation) is now known to be the cause for transfer of acoustic energy from blade passing harmonics to other engine orders [11]. Such sub-blade passing tones are called multiple pure tones, or buzzsaw noise.

Fan tonal noise was first characterized by Tyler and Sofrin [10] and since then substantial research on the topic has led to a very good understanding of the noise generation mechanisms as well as development of a few noise reduction technologies (e.g., varying vane count, lean, and sweep) [8]. Furthermore, Gliebe [11] showed that if one could completely eliminate all fan tones, total system noise would be reduced by 0.5 to 1.5 EPNdB (effective perceived noise level in dB), depending on the operating condition. EPNdB is a noise metric that accounts for human subjective annoyance including penalty for tone protrusion. The limited impact of fan tonal noise on EPNdB as well as the recent advances in mitigating tonal noise has rendered fan broadband noise to be the largest contributor to overall noise from an aircraft, and is therefore the focus of this research.

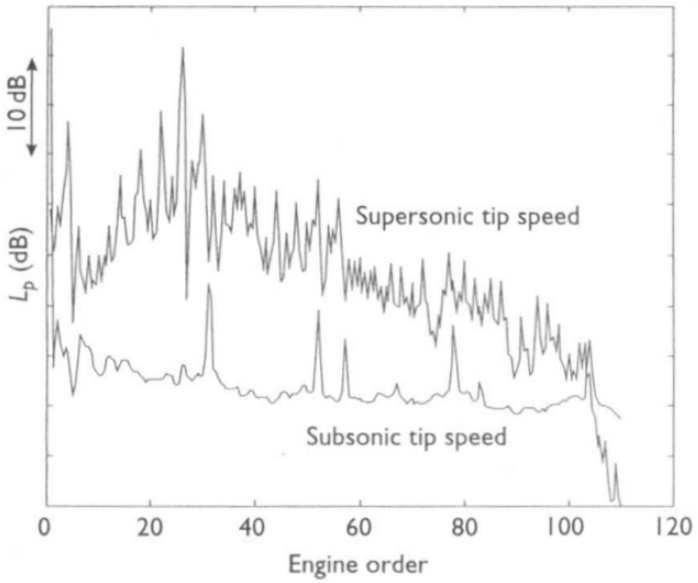

Figure 2.2: Typical far field sound pressure level spectra for two different rotor tip speeds (reproduced from Joseph and Smith [2]).

Fan Broadband Noise

Broadband noise is generated by flow turbulence. Broadband noise generated anywhere in the fan-OGV (outlet guide vane) stage is referred to as fan broadband noise. There are multiple sources of fan broadband noise, which originate due to different physical mechanisms. Free turbulence, e.g., in blade wakes, is not effective at radiating sound. However, interaction of turbulence with solid surfaces generates unsteady pressure (loading), which is an efficient noise radiation source. In a fan-OGV stage, turbulence comes about from various sources: ingested with inflow, boundary layer on inlet duct, rotor and OGV blade surfaces, rotor blade tip vortex, and velocity shear in blade wakes. These different sources of turbulence interact with rotor and OGV blade surfaces and generate noise. These noise sources are distributed over large areas of dynamically loaded surfaces, which makes it challenging to isolate noise radiating regions for active or passive treatment. Currently, passive mitigation is used in the form of liners (Helmholtz resonators), applied on engine inlet and outlet ducts, that mitigate noise by converting it into heat.

In relatively recent past, there have been two experimental campaigns undertaken to investigate source characteristics of fan broadband noise. To author's knowledge, these are the only publicly available fan noise datasets for realistic geometries. The measurements in both experimental campaigns include very detailed aerodynamics and acoustics data. The findings from these experiments as they relate to noise source characteristics are summarized in the next two sections.

Boeing 18-inch Fan Rig Test

Ganz et al. [3] used an 18-inch fan rig, representative of modern high-bypass ratio turbofan, in the Boeing's Low-Speed Aeroacoustic Facility (LSAF) to characterize fan broadband noise sources. The experiments were carefully crafted to vary different parameters (and geometry) to enable isolation and quantification of different fan broadband noise generation mechanisms. Figure 2.3 shows a schematic of the fan rig and lists the different noise sources that were

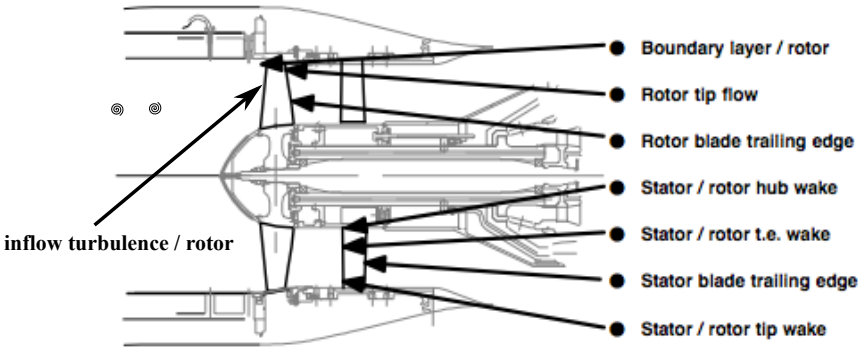

Figure 2.3: Schematic of the Boeing 18" fan rig. Also listed are the potential fan broadband noise sources in a fan stage that were investigated (reproduced from Ganz et al. [3]).

investigated [3]. The noise generation mechanism behind each of these sources are summarized below. These have been grouped into two broader categories.

1. **Interaction Noise Sources:**

   Sources grouped in this category arise from interaction of ingested turbulence or turbulence that is generated by a surface *different* from the surface with which it interacts to produce noise.

   - *Boundary layer/rotor:* As air flows through the inlet, boundary layer develops on the inside of the duct (casing). The thickness of this boundary is usually larger than the gap between the rotor (fan) tip clearance. The turbulence in the casing boundary layer interacts with the rotating fan blade tips and generates noise. This broadband noise is modulated with the rotation frequency of the blades and hence the spectra show broadened peaks at BPF and its harmonics. Also, this noise source radiates primarily through the inlet because fan blade passages are typically choked (in passage shock) near the tip for most operating conditions.
   - *Stator/rotor trailing edge wake:* Turbulence generated in the viscous wake of the rotor convects with the flow and impinges on the downstream stator. Figure 2.4 shows the viscous wake of an airfoil. The wake can be decomposed into a mean velocity deficit (time independent in airfoil frame of reference) and a time-dependent, fluctuating (turbulent) velocity component. The interaction of mean velocity deficit

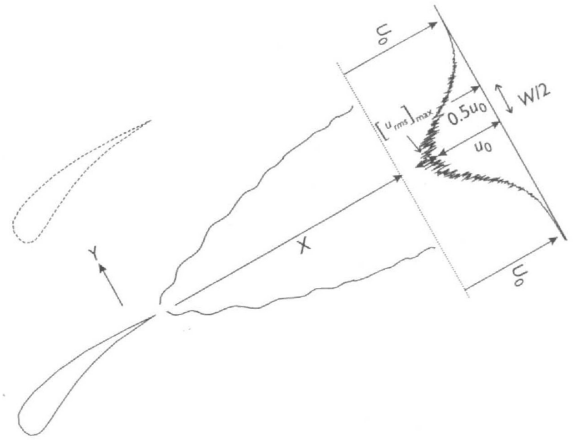

Figure 2.4: Mean and turbulence characteristics of airfoil wake (reproduced from Joseph and Smith [2]).

with downstream stator produces tonal noise at blade passing frequencies, while the interaction of turbulent fluctuations results in broadband noise.

Noise thus produced at the stator blades radiates both upstream and downstream. The upstream radiated noise has to first pass through the rotor, where interesting physical phenomena such as frequency scattering occur. Aft-radiated noise transmits through the duct in the presence of mean flow and then radiates out. Aft-radiated noise has to go through the shear layer created by the jet exhaust, which causes diffraction (bending) of acoustic waves.

- *Stator/rotor hub wake* and *Stator/rotor tip wake:* Secondary flows in the rotor bladerow are prominent near the tip and the hub. Turbulence is generated in these secondary flows, which convects downstream and produces noise upon interaction with the stator.

- *Rotor/inflow turbulence:* Freestream turbulence is ingested into the engine along with the flow. Interaction of this turbulence with the fan produces noise that radiates primarily through the inlet. This noise is predominantly broadband in nature, but the same mechanism can also produce tonal noise as explained below. At takeoff, when flight speed is low but thrust requirement is high, large streamtube contraction occurs. Turbulent eddies that are isotropic in farfield get elongated in streamwise

direction as they get ingested by the rotor. Chopping of such elongated eddies by multiple fan blades can also result in tonal noise at blade passing frequencies [12].

2. **"Self" Noise Sources**

   Viscous flow over surfaces generates boundary layer, which becomes turbulent if the Reynolds number is sufficiently high. Turbulence in the boundary layer interacts with the same surface over which the fluid is flowing. The noise produced by such interaction is termed "self" noise. Three different self noise sources are possible in a fan stage.

   - *Rotor blade trailing edge* and *Stator blade trailing edge:* Interaction of blade (rotor or stator) boundary layer with the same blade surface produces broadband noise. While the entire blade surface experiences turbulent pressure fluctuations (unsteady lift), it is the trailing edge of the blade that becomes the primary radiator of noise. The energy in the hydrodynamic turbulence (vorticity) scatters into acoustic fluctuations at the trailing edge singularity, thus making the trailing edge a more dominant noise source than the rest of the blade surface.
   - *Rotor tip flow:* Turbulence generated in the secondary flow (tip vortex) interacts with the top edge of the rotor blade and generates noise.

In these experiments [3], three fan broadband noise sources were observed to be prominent: (1) rotor self noise, (2) rotor-stator (fan-OGV) interaction noise, and (3) rotor-boundary layer interaction noise. Figure 2.5 shows the breakdown of the total inlet- and aft-radiated noise into these three sources. *According to this data, rotor-stator interaction is the dominant (although by only a few dBs) source of broadband noise in a turbofan engine.* This is the key result of Ganz et al. [3].

NASA Source Diagnostic Test

A similar detailed experimental study called the Source Diagnostic Test (SDT) was carried out by NASA [13, 14, 15, 16, 4, 17]. As the name suggests, the purpose of the tests was to diagnose fan noise sources. The tests were conducted inside the 9' × 15' Low Speed Wind

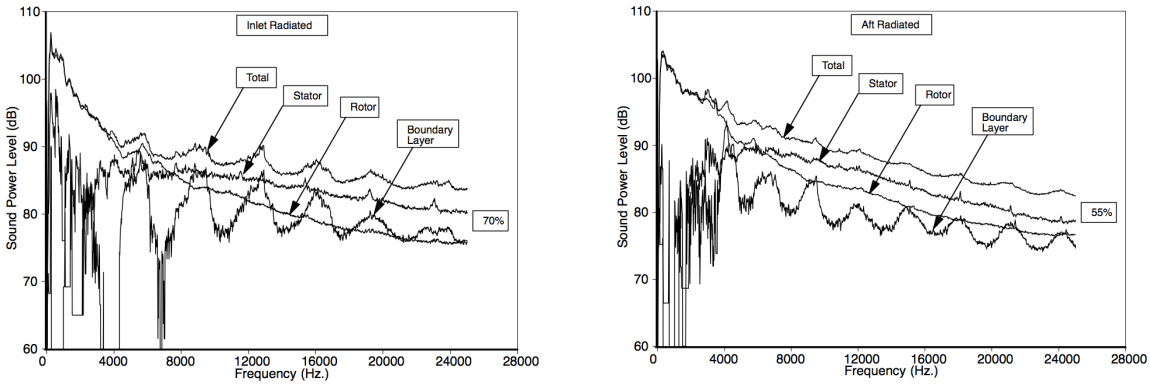

(a) Inlet radiated

(b) Aft radiated

Figure 2.5: Total fan broadband noise spectrum and its decomposition into contributing sources for (a) inlet radiated, and (b) aft radiated noise. (reproduced from Ganz et al. [3])

Tunnel (LSWT) at NASA Glenn Research Center. A 1/5th scale model of a fan bypass stage of a modern high bypass ratio turbofan engine was used. They tested two rotor (fan) geometries designated "R4" and "M5" in combination with three stator geometries, as well as one without a stator. Aerodynamic performance measurements were made for aerodynamic performance using total pressure and total temperature rakes. Fan wakes were measured using hotwire and Liquid Doppler Velocimetry (LDV) techniques in the gap between the fan and the outlet guide vane. Acoustic measurements were made using in-duct Kulites and far-field sound was measured with a traversing probe on a straight-line arc. Figure 2.6 is a schematic showing far-field noise measurement probe with respect to the fan rig.

Geometries and Configurations

The three stator (OGV) geometries were used in these tests were designated *Baseline*, *Low-count*, and *Low-noise*. Baseline OGV consisted of 54 narrow-chord vanes, Low-count OGV of 26 wide-chord vanes, and Low-noise OGV had 26 wide-chord vanes with 30° aft sweep. Figure 2.7 shows schematic diagrams and pictures of the three stator geometries tested during the SDT campaign. A fan configuration without any stator was also tested with the intent to measure noise due to "rotor alone" and thus, in principle, allow calculation of noise due to rotor-stator interaction (by subtracting "rotor alone" noise from "stage" noise measurements).

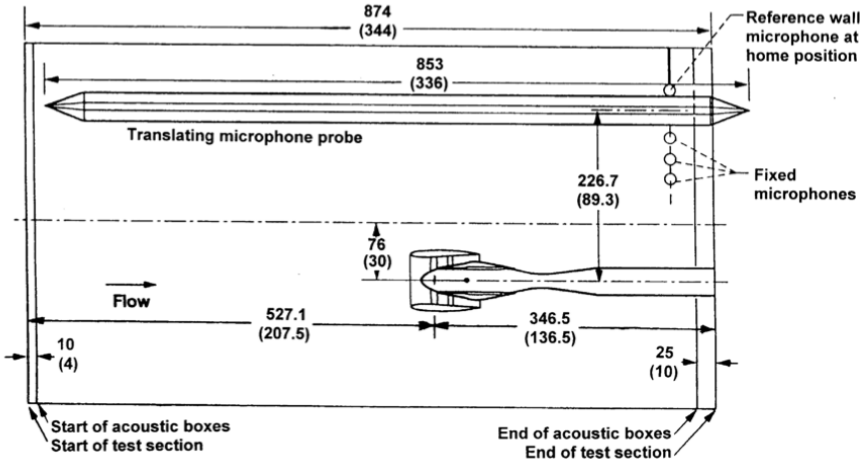

Figure 2.6: Schematic showing the fan rig and the far-field noise measurement probe in the LSWT facility. (reproduced from Woodward et al. [4])

An external support system was designed to hold the nacelle in place (maintaining fixed fan clearance) to test the rotor-alone configuration. In the rotor-alone configuration, the area of the fan nozzle was varied to achieve the same fan performance as in the rotor-stator configurations. Figure 2.7 also shows the schematic of rotor-alone configuration along with the rotor and the external support for nacelle. The attempt to decompose fan noise into rotor alone and rotor-stator interaction components using the rotor-alone configuration test data was only partly successful though due to the extraneous noise sources in the rotor-alone configuration arising from swirling flow impinging on the downstream strut and additional flow scrubbing noise.

Data Processing

The raw acoustic data from the experiments is processed to identify broadband noise and decompose it into contributions from rotor alone and rotor-stator interaction noise sources. Sideline (far-field) acoustic pressure data is integrated over all the microphones to compute sound power (intensity flux). Figure 2.8 shows sound power spectra at various steps during the decomposition process. Firstly, the tones at the fundamental and the harmonics of BPF are filtered out. A low-pass filter is then applied to smoothen the spectra. In the figure, these steps are only shown for one configuration where both rotor and stator are present. This configuration is denoted as "R+S" in the figure. Noise spectra from rotor alone configuration

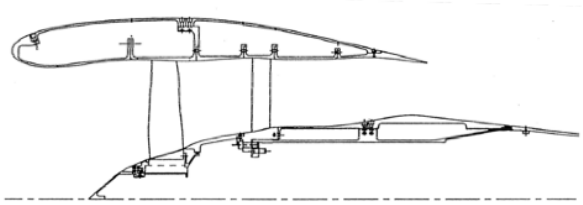

(a) Schematic of R4-Baseline OGV

(b) Baseline OGV

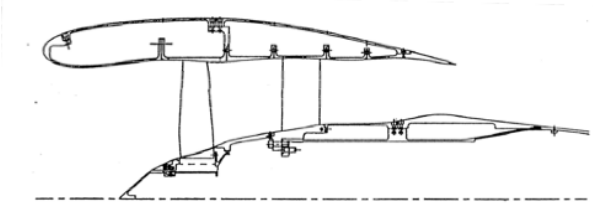

(c) Schematic of R4-Low-count OGV

(d) Low-count OGV

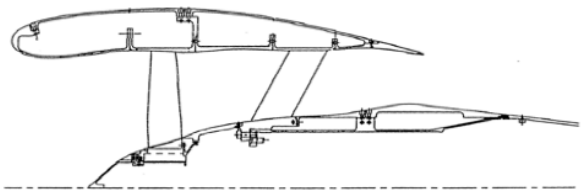

(e) Schematic of R4-Low-noise OGV

(f) Low-noise OGV

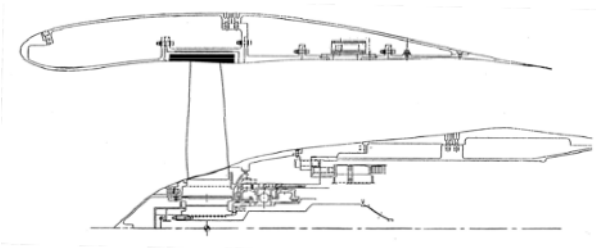

(g) Schematic of rotor alone

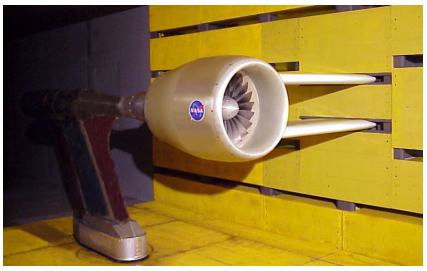

(h) External support for rotor alone

Figure 2.7: Different fan-stator combinations tested as part of the SDT campaign. (reproduced from Woodward et al. [4])

are processed in similar manner; these are denoted "RA" for rotor alone. Contribution from rotor-stator interaction noise is then estimated by logarithmic subtraction of "RA" noise from "R+S" noise. This is of course an approximation, which is found to break down for many cases. Figure 2.8 shows that the sound power from "R+S" configuration is greater that "RA" configuration only for frequencies between 1 BPF and 4 BPF. At other frequencies, the rotor-alone configuration, which theoretically contains fewer sources, radiates more sound than the rotor-stator configuration. This anomalous observation is attributed to the additional noise sources in the rotor-alone configuration from interaction of swirling flow with downstream strut, and increased flow scrubbing noise. Therefore, for further comparative analysis, tone-removed and smoothened "R+S" sound power data is used.

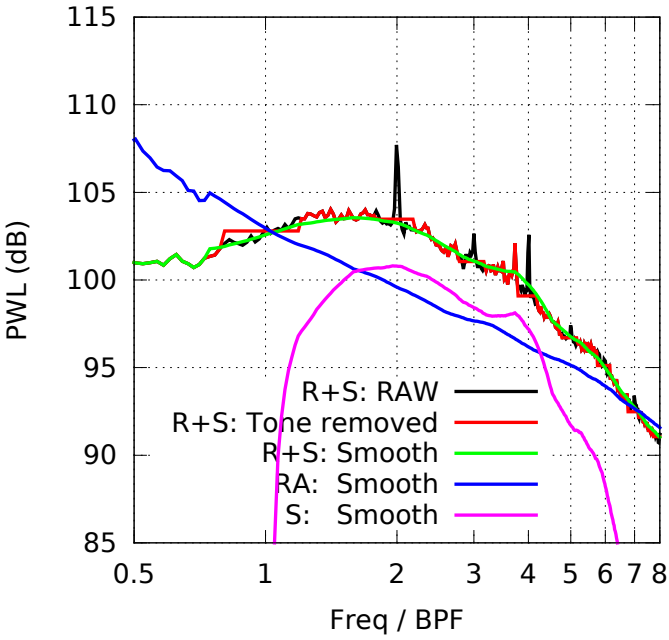

Figure 2.8: Sound power spectra at various stages of processing of data.

Speed Scaling

Processed sound power spectra at six different fan speeds are plotted with different normalizations in Fig. 2.9 to estimate speed scaling of fan noise. The different curves on these plots

correspond to different fan speeds, expressed as percentage of the design fan speed. The primary noise generation mechanism is believed to be unsteady lift (dipole source) on the blades (rotor as well as stator) generated due to the interaction of turbulence with blade surfaces. The sound intensity radiated by an unsteady-force noise source is expected to scale with fifth power of flow Mach number, $|\mathbf{I}| \propto M^5$, from theory based on dipole source assumption. Sound power is computed as, PWL $= 10 \log_{10} \int \mathbf{I} \,.\, d\mathbf{S}$. Effect of Mach number can be removed from the PWL by subtracting out $50 \log_{10} M$.

Scaling with different power of Mach number (0, 2, 3, and 5) are plotted in Fig. 2.9 to check if M^5 collapses the data. However, the different spectra seem to collapse best with M^3 scaling for sound spectra as opposed to M^5. This could be because a fan is designed to operate at flow incidence that optimizes performance at design point. As the operating speed is changed, the incidence angle changes, which changes the turbulence intensity and the mean velocity deficit in the blade wake. This change in turbulence intensity with Mach number can perhaps explain the M^3 scaling observed in the data.

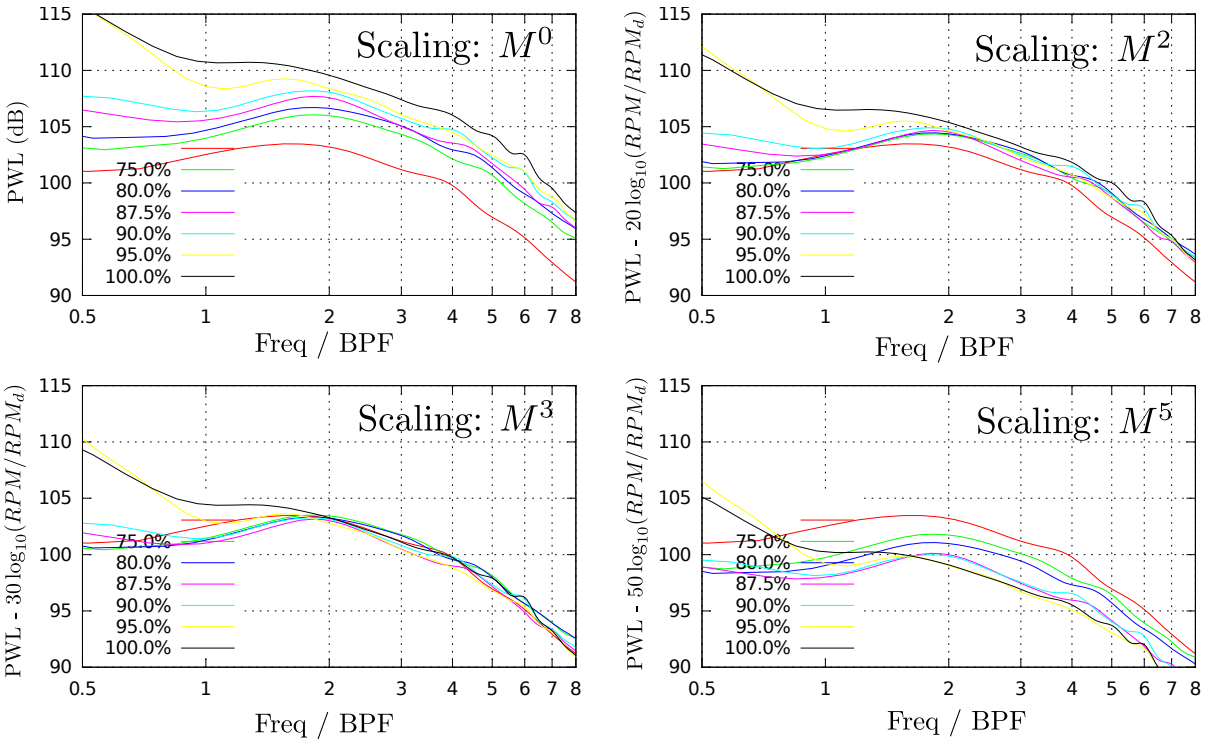

Figure 2.9: Speed scaling: M^3 seems to collapse the spectra better than M^5.

Vane-count Scaling

By analyzing the acoustic data from Baseline (54 vanes) and Low-count (26 vanes) OGV geometries, we can deduce the scaling of sound power with number of vanes in the OGV bladerow. To maintain aerodynamic similarity, the solidity (chord-to-gap ratio) is kept the same between the two OGV geometries. Hence the chord of the Low-count vanes is bigger by a factor 54/26.

Figure 2.10 plots the un-scaled (top row) and scaled (bottom row) sound power spectra for Baseline and Low-count OGV. The scaling used is PWL $\propto 10\log_{10}(N_V)$, where N_V is the number of vanes in the OGV. All the plots show that for frequencies greater than 2×BPF, the spectra reasonably collapse with $10\log_{10}(N_V)$ scaling. As can be expected from length scales involved, cascade effects are important at low frequencies (large length scale), whereas for high frequencies (small length scale), each vane responds independently of the neighboring vanes. Scaling with vane count depends on two factors: (1) scaling of turbulence spectra which gets scattered into "cut-on" (radiating) acoustic modes, and (2) scaling of cascade response to a gust. These two factors vary with frequency and as can be observed in Fig. 2.10. At low frequencies, the sound power spectra do not vary with vane count, while at mid-to-high frequencies, the spectra scale approximately as $10\log_{10}(N_V)$. Care needs to be taken when deducing much out of these plots for low frequencies, as it is possible that the rotor-alone noise dominates here and hence no variation with vane count is observed.

Effect of Vane Sweep

The SDT data reveals the effect of sweeping the OGV. The Low-noise OGV is a 26-count swept OGV, with the same vane count as the Low-count OGV. Comparing the measured noise data from these two configurations gives a measure of vane-sweep effect. Figure 2.11 compares sound power spectra for Low-count and Low-noise OGVs at three different fan speeds. Physically, it is expected that sweep will further de-correlate (span-wise) the noise sources on the blade and hence some noise reduction is expected. For low fan speeds some reduction in

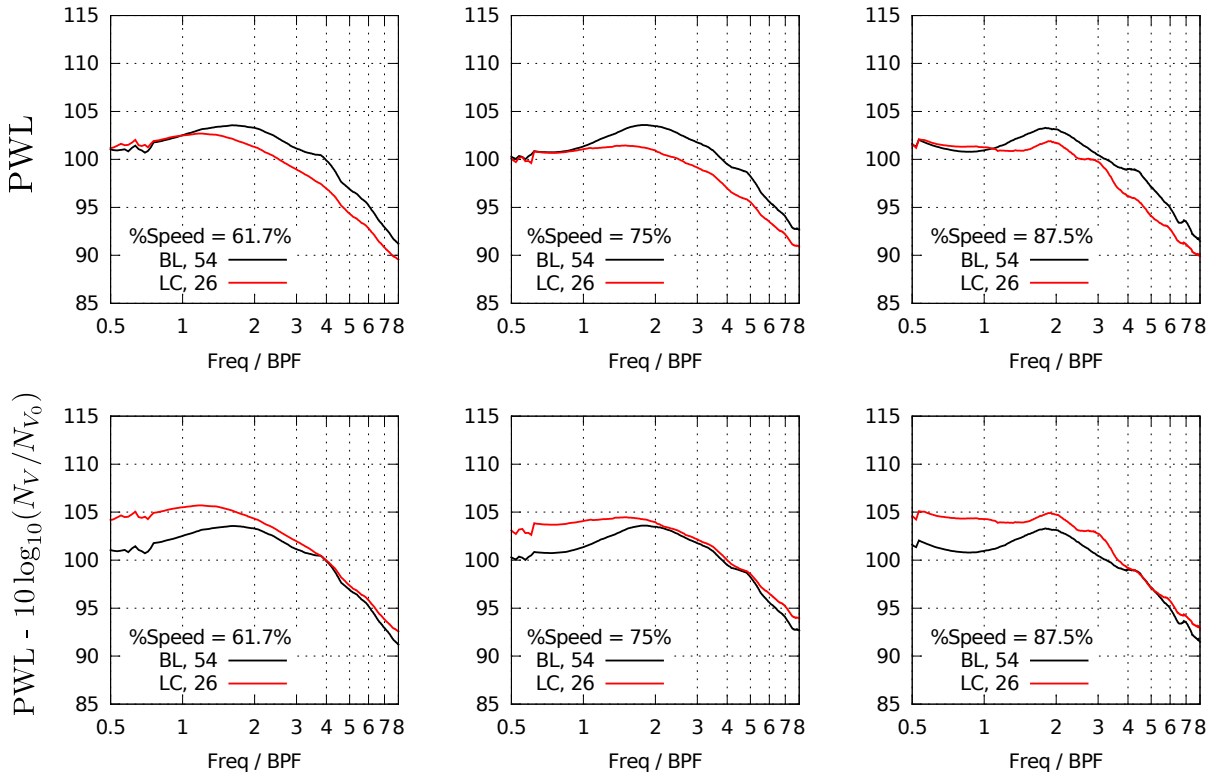

Figure 2.10: Vane count scaling: $PWL \sim 10\log(N_V)$ seems to collapse the mid- to high-frequency spectra.

sound power level (of the order $1-2$ dB) is observed. However, at higher fan speeds there is no significant reduction.

Theoretical Background

This section discusses various theoretical aspects of the overall problem.

Aerodynamic Noise Generation

Modern aeroacoustic theories are derived primarily from the classical work by Sir James Lighthill [18, 19]. He cleverly re-arranged the governing flow equations to obtain the wave equation (Eq. 2.1), written here for fluctuating component of density ($\rho' = \rho - \rho_0$) as

$$\left[\frac{\partial^2}{\partial t^2} - c_0^2\nabla^2\right]\rho' = \frac{\partial^2 T_{ij}}{\partial x_i\,\partial x_j}. \tag{2.1}$$

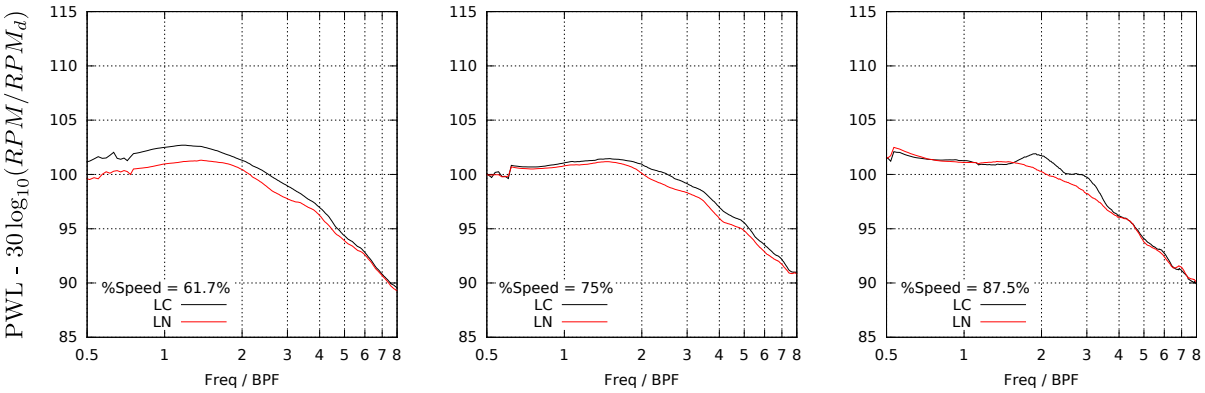

Figure 2.11: Effect of vane sweep (30^o aft sweep)

In Eq. 2.1, $T_{ij} = \rho u_i u_j + p_{ij} - c_0^2 \rho' \delta_{ij}$ is called the Lighthill stress tensor. Here, $p_{ij} = \delta_{ij} p' - \tau_{ij}$, where δ_{ij} is the Kronecker delta function, τ_{ij} represents viscous stress, u_i is the ith component of instantaneous flow velocity and ρ is the total density. For homentropic flows, $p' = \rho'/c_0^2$. The term in brackets on the l.h.s. of Eq. 2.1 is the standard wave operator (free space, quiescent medium); the r.h.s. therefore represents the aerodynamic noise sources. The problem of solving for noise from the flow field (non-linear equations) is thus cast as an equivalent problem of solving the linear wave equation (much simpler). This equivalent problem formulation is called the Lighthill's acoustic analogy. Several variants of Lighthill's acoustic analogy incorporating effects of meanflow, presence of solid bodies etc. are now available and used in aeroacoustic applications.

Eq. 2.1 can be solved using Green's functions [18]. The 3-D, free-space Green's function for the wave equation is the solution of

$$\left[\frac{\partial^2}{\partial t^2} - c_0^2 \nabla^2\right] g(\mathbf{x}|\mathbf{y}; t|\tau) = \delta\{\mathbf{x} - \mathbf{y}\}\delta\{t - \tau\}. \tag{2.2}$$

Eq. 2.2 represents wave equation for an impulsive (represented by the Dirac delta function) source located at $\mathbf{y}$ in space and at τ in time. The solution of Eq. 2.2 is the free-space (3-D) Green's function which is known to be

$$g(\mathbf{x}|\mathbf{y}; t|\tau) = \frac{\delta\{|\mathbf{x} - \mathbf{y}| - c_0(t - \tau)\}}{4\pi c_0 |\mathbf{x} - \mathbf{y}|}. \tag{2.3}$$

The solution for any arbitrary distribution of source, say $f(\mathbf{y},\tau)$, is obtained by convolving $f(\mathbf{y},\tau)$ with the Green's function –

$$\begin{aligned}\rho'(\mathbf{x},t) &= \int_{\mathbf{y}}\int_{\tau} g(\mathbf{x}|\mathbf{y};t|\tau)f(\mathbf{y},\tau)\ \mathrm{d}\tau\ \mathrm{d}\mathbf{y} \\ &= \int_{\mathbf{y}}\int_{\tau} \frac{f(\mathbf{y},\tau)\delta\{|\mathbf{x}-\mathbf{y}|-c_0(t-\tau)\}}{4\pi c_0|\mathbf{x}-\mathbf{y}|}\,\mathrm{d}\tau\ \mathrm{d}\mathbf{y}\end{aligned}$$

Solution to Lighthill's equation can thus be written as

$$\rho'(\mathbf{x},t) = \int_{\mathbf{y}}\int_{\tau} \frac{\dfrac{\partial^2 T_{ij}(\mathbf{y})}{\partial y_i\,\partial y_j}\delta\left\{|\mathbf{x}-\mathbf{y}|-c_0(t-\tau)\right\}}{4\pi c_0|\mathbf{x}-\mathbf{y}|}\,\mathrm{d}\tau\ \mathrm{d}\mathbf{y}. \tag{2.4}$$

The integral over τ can be evaluated using properties of Generalized functions. Using some properties of convolution integrals, the density fluctuations at observer location $\mathbf{x}$ and time t can be obtained as

$$4\pi c_0^2\rho'(\mathbf{x},t) = \frac{\partial^2}{\partial x_i\,\partial x_j}\int_{\mathbf{y}} \frac{T_{ij}\left(\mathbf{y},t-r/c_0\right)}{r}\,\mathrm{d}y, \tag{2.5}$$

where $r = |\mathbf{x}-\mathbf{y}|$. The volume integral (over the source region $\mathbf{y}$) requires the knowledge of the Lighthill stress tensor in the entire source region (3-D volume). This essentially means that both temporal and spatial distributions of the turbulence in the source region are required to solve Lighthill's equivalent/analogical problem. If that is to be evaluated numerically by solving the flow equations (e.g., LES or DNS), there is little benefit of the acoustic analogy. Tremendous computational savings are realized however if the source term can be modeled using reduced-order (RANS etc.) flow calculations.

Lighthill's acoustic analogy is for aerodynamic sources in free space (e.g., noise generated by jet flows). In flows over solid bodies, the interaction of the fluid with the surface also produces noise. The effect of solid boundaries was incorporated by Curle [20] and one form of the general acoustic analogy is given by Eq. 2.6:

$$4\pi c_0^2\rho'(\mathbf{x},t) = \underbrace{\frac{\partial^2}{\partial x_i\,\partial x_j}\int_V \left[\frac{T_{ij}}{r}\right]_\tau \mathrm{d}V}_{I} + \underbrace{\frac{\partial}{\partial x_i}\int_S \left[\frac{n_j}{r}\left(\rho u_i u_j + p_{ij}\right)\right]_\tau \mathrm{d}S}_{II} - \underbrace{\frac{\partial}{\partial t}\int_S \left[\frac{n_j}{r}\frac{\partial(\rho u_j)}{\partial t}\right]_\tau \mathrm{d}S}_{III}. \tag{2.6}$$

In Eq. 2.6 the terms in the square brackets should be evaluated at source time, $\tau = t - r/c_0$. The three terms, I, II, and III in Eq. 2.6 respectively represent three different fundamental sound sources: quadrupole (associated with unsteady stresses), dipole (unsteady forces), and monopole (unsteady mass). Ffowcs Williams and Hawkings [21] added the effect of moving boundaries to this and the resulting formulation, popularly known as the Ffowcs Williams-Hawkings (FW-H) equation, is the most widely used acoustic analogy for numerical aerodynamic noise prediction. The form of the FW-H equation typically used in low Mach number flows ignores the volume integral and is written as

$$\begin{aligned} 4\pi \left|\mathbf{x}\right| c_0^2 \rho'(\mathbf{x},t) &= \frac{x_i}{c_0 \left|\mathbf{x}\right|} \frac{\partial}{\partial t} \int \left[p' n_i + \rho u_i (u_j - U_j) n_j\right] \, \mathrm{d}S \\ &+ \frac{\partial}{\partial t} \int \left[\rho_0 u_i + \rho'(u_i - U_i)\right] n_i \, \mathrm{d}S. \end{aligned} \tag{2.7}$$

Time-accurate information of flow variables $\rho, \mathbf{u}$, and p are required over a surface (denoted by S in Eq. 2.7 enclosing all the sources of sound in the problem. This data is typically obtained numerically through U-RANS or LES calculations. The surface S can be *permeable* (allowing flow through it) or *solid* (if only dipole surface sources are important).

Scaling of the fundamental noise sources (mono-, di-, and quadrupole) can be derived using dimensional analysis of the respective terms in Eq. 2.6. For a compact source (source length scale small compared to wavelength), far-field acoustic intensities for quadrupole, dipole and monopole sources scale as M^8, M^6 and M^4 respectively. Lighthill demonstrated the M^8 scaling of noise from a compact turbulent eddy in a cold, subsonic jet. This relation is now known as the "eighth power law" of jet noise. Curle [20] demonstrated the scaling for a compact dipole source. These scaling laws, as seen before, can help in understanding the nature of sound sources from experimental data.

Fan Broadband Noise

Through experiments it has been identified that rotor-stator interaction is the dominant source of fan broadband noise. Rotor trailing edge noise is a close second. "Strip theory" is a standard approach that is routinely used in analyzing these sources. The noise generating bladerow is discretized into many annular strips (cascade). The annular cascade is typically

"flattened out" to a rectangular cascade to permit 2-D analysis. For small wavelengths (compared to distance between neighboring airfoils in a cascade), cascade effects can be ignored and single airfoil response is sufficient.

Both rotor-stator interaction and trailing edge noise sources can be fundamentally understood by studying noise due to interaction of flow turbulence with a cascade or a single airfoil. In the case of trailing edge noise, the turbulence is generated in the airfoil boundary layer. In the case of rotor stator interaction, the turbulence is generated upstream of the noise producing airfoil. This sections provides some characteristics as well as approaches to model these two noise generation mechanisms.

Trailing Edge Noise

When turbulent flow goes over a lifting surface, it produces unsteady pressure on the surface, which can be considered as dipole sources given by the second integral of Eq. 2.6. Dimensional scaling suggests that sound power from this interaction scales with flow Mach number as M^6. However, experimental data for noise from an airfoil in freestream [22] has shown a M^5 scaling, which is larger than M^6 for subsonic flows. Ffowcs Williams and Hall [23] analytically proved that the presence of a sharp edge (e.g., airfoil trailing edge) is the cause of this amplification. They [23] investigated flow over a rigid half plane and demonstrated that a sharp edge significantly amplifies the radiated sound from the turbulent eddies that are close (distance much smaller than wavelength) to the edge.

There has been a large body of work [24, 25, 26, 27, 28] in the area of airfoil trailing edge noise as it is perhaps the most important noise source mechanism in airframe noise and wind turbine noise. The work offers explanation to the nature of the noise, its propagation into free space and the generation mechanism itself based on theory and various types of computational methods. There are also examples of works [29, 30] showing noise reduction by modifying the trailing edge by using, for example, brushes and serrations. The main focus of this research is going to be on interaction noise and therefore only the salient feature of trailing edge noise, which is the M^5 scaling is mentioned here.

Interaction Noise

The focus in this section is on noise generated due to turbulent wake (presumably produced by upstream rotor cascade) interacting with a stator cascade. Figure 2.12 shows a schematic of the problem where the stator airfoils are represented by unloaded flat plates. The analysis assumes that the turbulence convects as a 'frozen' gust. 'Frozen' implies that the turbulence spectrum does not evolve with space or time; it simply convects with the flow. The analysis is carried out in the frequency domain and hence the incident turbulent gust is written as a sum of harmonic wave components. Cascade / airfoil response from each harmonic component gust is then independently carried out.

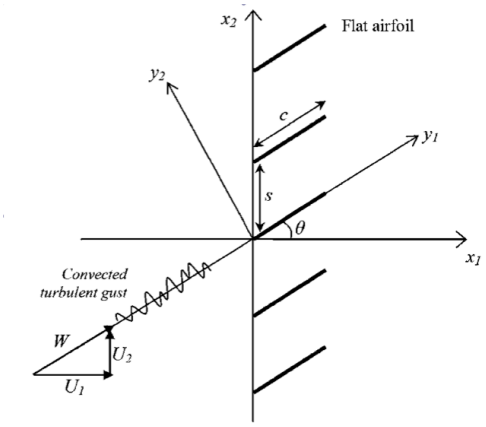

Figure 2.12: Schematic of turbulent gust and a flat-plate cascade (reproduced from Cheong et al. [5]).

Consider a harmonic gust of the form

$$\mathbf{u} = \mathbf{u_0} \exp\left[j(\mathbf{k}.\mathbf{y} - k_1 W_1 t)\right], \tag{2.8}$$

where, $\mathbf{u_0}$, is the gust amplitude, $\mathbf{k}$ is the gust wavenumber, $\mathbf{W}$ is the velocity vector, and $\mathbf{y}$ defines the blade-fixed coordinate system. For this oncoming gust, the lift response of a single, flat-plate airfoil can be written, as given by Goldstein [31], as

$$F_2 = \pi \rho_0 c W_1 u_{02} \exp\left[j(k_2 y_2 - k_1 W_1 t)\right] \; \Gamma(k_1, k_2, M_1), \tag{2.9}$$

where c is the airfoil chord, u_{02} is the upwash velocity magnitude, and Γ is the non-dimensional airfoil response function. For a continuous frequency and wavenumber spectrum the overall

response is given in terms of power spectral density, defined as mean square force per unit length per unit radian frequency [32, 31], is

$$S_{FF}(\omega) = \pi^2 \rho_0^2 c^2 W_1 \int_{k_2} |(\Gamma(k_1, k_2, M_1))|^2 \left(\int_{-\infty}^{\infty} \Phi_{22}(k_1, k_2, k_3) \mathrm{d}k_3 \right) \mathrm{d}k_2, \tag{2.10}$$

where, $\Phi_{22}(k_1, k_2, k_3)$ is the wavenumber energy spectral density of the upwash velocity, $k_1 = \omega / W_1$, and the integral over k_2 should only be over wave numbers that result in cut-on acoustic modes. The 'frozen gust' assumption is crucial in the derivation of Eq. 2.10. The implications of assuming the airfoil to be an unloaded flat plate has been investigated. Lorence and Hall [33] showed that overall sound power levels are independent of airfoil camber and thickness. Evers and Peake [34] concluded that camber and thickness effects tonal noise but not broadband noise. Devenport et al. [35] carried out leading edge noise measurements and also calculations for three different airfoils. They found that angle of attack (hence mean loading) significantly affects airfoil response but not the leading edge noise; they attributed this to the averaging of isotropic turbulence spectrum.

Solution of Eq. 2.10 requires the airfoil response function $\Gamma(k_1, k_2, M_1)$. Note that for one operating point calculation, this has to evaluated for many frequencies (broadband), and for a very large number of k_2. An analytical (or semi-analytical) response function is therefore desirable to keep the computation cost in reasonable limits. The induction effect due to shed vorticity have to be accounted for in these calculations. Von Kármán and Sears [36] derived expressions for unsteady lift and moment due to airfoils in non-uniform motion using circulation theory of airfoils. Sears [6] applied the results to the case of translation and rotation of airfoil in steady uniform flow and the case of fixed airfoil in sinusoidally varying vertical gust.

This analysis assumes 2-dimensional airfoil and considers small airfoil thickness and small amplitude of oscillations. Lift and moment are expressed as contributions from three physical phenomena: quasi-steady, apparent-mass and wake effect. The quasi-steady loads are due to vorticity distribution on the airfoil, the apparent-mass loads are due to time varying behavior of this vorticity on the airfoil surface, and the wake effect is due to the downwash induced by the shed vorticity on the airfoil. Consider a single-harmonic gust (upwash velocity) given as

$$u_2(x, t) = u_{02} e^{i\nu(t - x/U)}, \tag{2.11}$$

where ν is the frequency of oscillations. The lift on the airfoil due to excitation by this gust is given by

$$L = \pi\rho c U u_{02} e^{i\nu t}\{[J_0(\omega) - iJ_1(\omega)]\, C(\omega) + iJ_1(\omega)\}, \tag{2.12}$$

where J_0 and J_1 are Bessel functions of first kind, and $C(\omega) = K_1(i\omega)/\left[K_0(i\omega) + K_1(i\omega)\right]$ where K_0 and K_1 are modified Bessel functions of the second kind. Figure 2.13 plots the variation of lift (normalized by $\pi\rho c U W e^{i\nu t}$) with reduced frequency, ω $(= \nu c/(2U))$. Note that the magnitude of L represents the absolute value of the lift and the phase represents the lag (time delay) in the airfoil response.

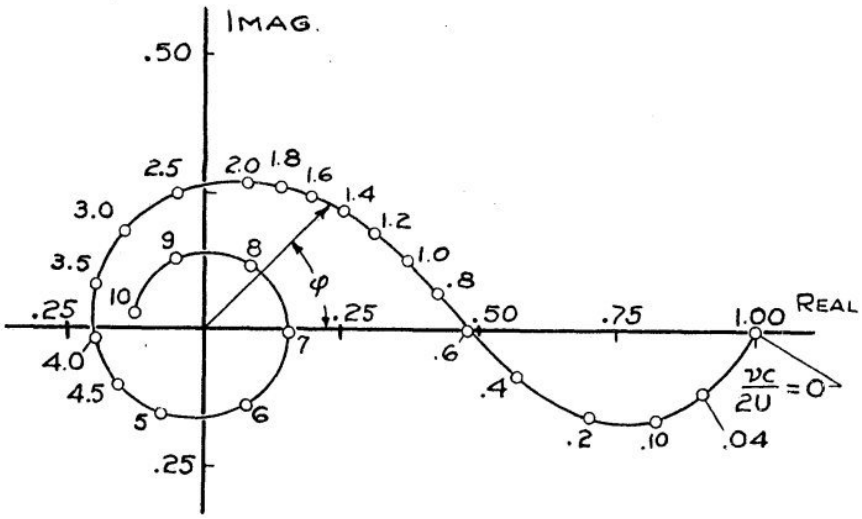

Figure 2.13: Vector diagram of normalized lift (reproduced from Sears [6])

The analysis can be extended to three-dimensional turbulent flow field by incorporating wavenumber components in the other two directions. Using a comparative study, Kobayashi [37] showed that two-dimensional analysis to compute unsteady forces is sufficient for fan noise prediction. Amiet [32] showed that a harmonic gust, at oblique incidence to the airfoil leading edge, will experience phase cancellation along the span and thus will produce considerably less lift compared to normal incident gust. Filotas [38] and Graham [39] analytically calculated aerodynamic response function for oblique gusts. Flow compressibility can appreciably change airfoil gust response. Graham [39] and Adamczyk and Brand [40] derived closed-form solutions for the compressible skewed-gust problem.

Solidity of modern turbomachine fan and OGV bladerows is reasonably high. For small frequencies (wavelength larger than spacing between blades), there is significant aerodynamic and aeroacoustic interaction between the neighboring blades of a bladerow. Therefore, in a strip theory analysis, the aerodynamic response to incident gusts has be computed for a cascade as opposed to a single airfoil. This restriction can be relaxed for very high frequencies where this aerodynamic interaction is insignificant. Two additional physical phenomena come into play when a gust-cascade (as opposed to gust-airfoil) is considered. Firstly, the upwash on an airfoil has to computed using induction from not just the shed vorticity of the given airfoil, but also the shed vorticities of neighboring blades. Secondly, passages between neighboring blades act as ducts; duct transmission phenomena such as cut-off (leads to "cascade resonance") therefore come into play. Smith [41] developed a theory for computing unsteady blade loading, vortical wave, and the upstream and downstream radiating acoustic waves due to harmonic gust interaction with a 2-D cascade of flat, unloaded plates. Whitehead [42, 43] developed a software called LINSUB using this theory, which has been widely used for fan noise prediction and validations of other methods.

Glegg [44] developed a procedure to compute 3-D rectilinear unloaded flat-plate cascade response due to 3-D gust. Cooper and Peake [45] incorporated swirling flow effects into their analysis and studied the effect of changing OGV sweep, lean and number of vanes. They predicted reduction in tonal noise for suitable sweep and lean, and also predicted broadband noise reduction due to reduction in number of stator vanes.

Figure 2.14 shows the variation of unsteady lift coefficient with respect to reduced frequency. In this figure, the unsteady lift is computed using the LINSUB code (shown as rectilinear cascade response), as well as using the incompressible [6] and compressible [40] Sears functions. The cascade response shows a sharp discontinuity indicating cascade resonance (mode cut-off) around $\sigma = 1.8$. Single-airfoil response functions don't exhibit this. Compressibility effects start to become important for $\sigma M_1 > 1$, which corresponds to $\sigma > .33$ in Fig. 2.14 ($M_1 = 0.3$ here). $\sigma M_1 = 1$ identifies the frequency above which the time taken for sound to propagate across the blade chord roughly equals the period of oscillation.

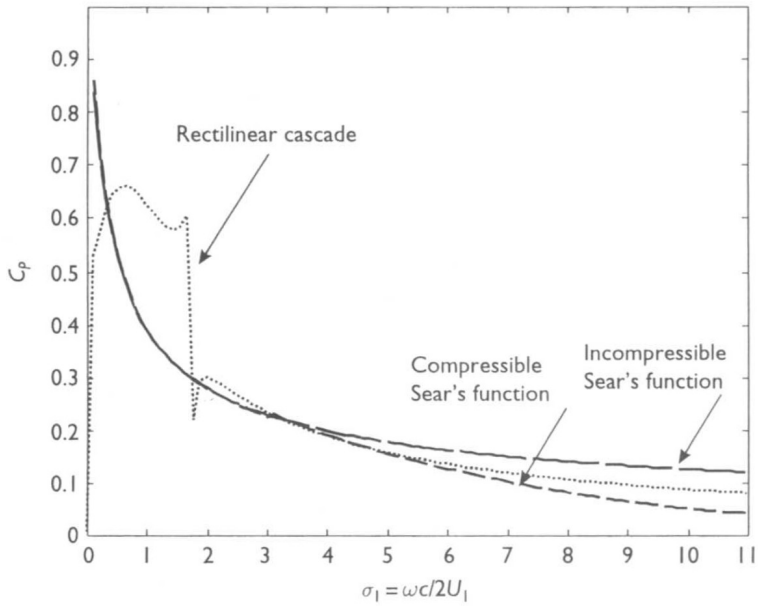

Figure 2.14: Unsteady lift coefficient (reproduced from Joseph and Smith [2])

Cheong et al. [5] developed a rotor-stator interaction broadband noise prediction model using LINSUB as the kernel to solve for cascade response. They identified the existence of a "critical" frequency above which cascade response can be replaced by single-airfoil response without sacrificing accuracy. The formulation was used to perform parameter sweeps varying number of blades, stagger angle, gap-chord ratio and Mach number. The formulation assumes homogeneous and isotropic turbulence and uses the Liepmann turbulence model. Zhou and Joseph [46] numerically solved for broadband self-noise using a frequency domain method. They used thin airfoil theory for unsteady blade loading, used actual airfoil surface rather than mean-chord plane for integration of surface sources and considered the effect of relaxing the frozen-gust assumption. Posson et al. [47] extended Glegg's approach [44] using strip-theory with an unsteady blade loading rectilinear cascade response. They compared results with good and reasonable accuracy for upstream and downstream acoustic power respectively.

Duct Transmission and Radiation

Noise generated in the fan stage propagates through the duct (both inlet and exhaust) and then radiates out. For commercial aircraft engines, the inlet duct can be approximated to be

cylindrical and the exhaust duct approximated to be annular. The transmission of sound in a duct depends on the duct geometry as well as the meanflow. While upstream of the fan and downstream of the OGV, there is little swirl in the flow (at design point), the flow between the fan and the OGV is swirling. Because of the geometry, it is convenient to write the wave equation is written in cylindrical coordinates. The wave equation for uniform flow with Mach number M along the x direction is

$$\left(\frac{1}{c_0}\frac{\partial}{\partial t} + M\frac{\partial}{\partial x}\right)^2 p - \left[\frac{\partial^2}{\partial r^2} + \frac{1}{r}\frac{\partial}{\partial r} + \frac{1}{r^2}\frac{\partial^2}{\partial \theta^2} + \frac{\partial^2}{\partial x^2}\right] p = 0. \tag{2.13}$$

For hardwall cylindrical ducts, the solution of Eq. 2.13 for a single frequency ω can be written as a sum of normal (eigen) modes of the duct,

$$\hat{p}(\omega) = \sum_{m=-\infty}^{m=\infty} \sum_{n=0}^{\infty} A_{mn} e^{j(\omega t + m\theta - \alpha_{mn} k x)} J_m(\kappa_{mn} r). \tag{2.14}$$

where $j = \sqrt{-1}$, wavenumber $k = \omega/c_0$, m and n are integers and any combination $[m, n]$ gives a unique normal mode for the problem. J_m is the Bessel function of first kind of order m and the transverse mode wavenumber κ_{mn} is found as the roots of $J'_m(\kappa_{mn} a) = 0$, where a is radius of the duct. The axial wave number is $\alpha_{mn} k$ and the azimuthal wavenumber is given by m/r at any radius r. The wavenumber components and frequency are related by the dispersion relation,

$$(1 - M^2)\kappa_{mn}^2 + \left[\alpha_{mn} k (1 - M^2) + Mk\right]^2 = k^2,$$

which reduces to $\kappa_{mn}^2 + \alpha_{mn}^2 k^2 = k^2$ for $M = 0$. The no-flow case is sufficient to illustrate the main concepts and is assumed below. For a given frequency (or k), $\alpha_{mn} = \sqrt{1. - (\kappa_{mn}/k)^2}$ becomes imaginary for $\kappa_{mn} > k$. The acoustic mode $[m, n]$ then decays exponentially as it travels along the x-direction. This phenomenon is called *cut-off* and the frequency defined by $\omega_{mn} = c_0 \kappa_{mn}$ is called the cut-off frequency. For real α_{mn}, the mode travels unabated in a hardwall duct.

Non-uniform meanflow can significantly affect duct transmission characteristics. The linearized Euler equations give vortical, entropic and acoustic characteristics, which can be clearly delineated in uniform flows. That is not the case when the meanflow is swirling. Golubev and Atassi [48] studied duct wave propagation in presence of swirling flows and concluded that total

perturbation field can be divided into "nearly-convected" and "nearly-sonic" velocities which correspond to vorticity and pressure dominated modes respectively.

Second step in quantifying noise reaching the observer is the radiation of noise from the duct to the outside. This involves "scattering" of acoustic modes from the inlet/exhaust duct. Joseph and Morfey [49] computed non-dimensional modal directivity factors H_{mn} for semi-infinite, cylindrical and hard-walled ducts. H_{mn} is used in computing far-field acoustic pressure field as follows:

$$p_{mn}(R,\theta,\phi) = \bar{p}_{mn} H_{mn}(ka,\phi)(a/R)e^{j(m\theta - kR + \omega t)};\ \text{for } kR \gg 1, \tag{2.15}$$

where θ and ϕ are azimuthal and polar angles respectively. Tyler and Sofrin [10] solved for the case where the duct is terminated by an infinite rigid flange. Solving for un-flanged duct involves a Wiener-Hopf integral equation and was solved by Levine and Schwinger [50] for plane waves. Weinstein [51] extend the solution to higher-order modes. The predicted solutions for flanged and un-flanged cases agree with measurements for forward arc but not in the vicinity of sidelines for normalized frequencies which are away from cut-off frequencies. Rice [52] and Joseph and Morfey [49] approximately collapsed the radiation data and derived expressions for multi-mode far-field radiation. Glegg [53] developed a Green's function using the Wiener-Hopf technique and solved for boundary layer flow over backward and forward steps. He found that far-field sound has streamwise dipole and omni-directional nature at low and high frequencies respectively.

CHAPTER 3. AERODYNAMIC NOISE PREDICTION FOR A ROD AIRFOIL CONFIGURATION USING INCOMPRESSIBLE AND COMPRESSIBLE LARGE EDDY SIMULATIONS

A paper submitted to *Computers & Fluids*

Anupam Sharma and Bharat Raj Agrawal

Abstract

Noise produced by aerodynamic interaction between a circular cylinder (rod) and an airfoil in tandem arrangement is numerically investigated using large eddy simulations. The quasi-periodic shedding from the rod and the resulting wake impinging on the airfoil produce unsteady forces on the two geometries. These unsteady forces acts as sources of sound which radiates to the farfield. The pimpleFoam (part of OpenFOAM) and the Charles (developed by Cascade Technologies) solvers are chosen to carry out incompressible and compressible large eddy simulations (LES) respectively. The airfoil is set at zero angle of attack for the simulations. The flow conditions are specified by the Reynolds number based on the rod diameter, $Re_d = 48$ K, and the flow Mach number, $M_\infty = 0.2$. Comparisons with measurements are made for (a) mean and r.m.s. surface pressure on the rod, (b) mean and r.m.s. axial velocity profiles in the rod and airfoil wakes, (c) velocity spectra in the near field, and (d) far-field pressure spectra and directivity. Code-to-code comparisons are drawn for several flow quantities for which no measured data is available. Near-field, off-surface flow data from the Charles simulation, and on-surface airfoil pressure data from the pimpleFoam simulation are used with the Ffowcs Williams-Hawkings (FW-H) acoustic analogy [21] and Amiet's extension [32] of Curle's theory [20] respectively to predict far-field sound. Both approaches give good agreement with the

near-field aerodynamics and the far-field sound measurements. Such detailed one-to-one comparisons of aerodynamic and aeroacoustic predictions between compressible and incompressible large eddy simulations have not been attempted before for this problem.

Introduction

Aerodynamic noise is a by-product of most engineering machines, e.g., aircraft, gas turbines, household fans, etc. Noise can be either tonal, in which case the acoustic energy is limited to a few discrete tones, or broadband, in which case the energy is spread across a wide range of frequencies. Flow turbulence is often the source of broadband aerodynamic noise. The wide range of time scales of turbulent eddies results in noise that is produced over a wide range of frequencies. Until recently, such broadband noise sources were estimated using approximate models for the flow turbulence energy spectrum, which is typically scaled using the turbulence kinetic energy and the integral length scale in the problem. These parameters are obtained by solving the Reynolds Averaged Navier Stokes (RANS) equations, which are computationally much less expensive to solve than simulations that resolve every minute detail in the flow (e.g., Direct Numerical Simulations). Large-scale computing has now become available to researchers, which allows direct computation of the full range of length and time scales important for sound generation and propagation. Such an approach gets get rid of the modeling assumptions required in simpler models and thus provides more accurate predictions. The Large Eddy Simulation (LES) technique is one such computational method that is becoming increasingly popular for noise prediction from engineering machines. Direct noise computation of a model engineering problem is attempted here using LES.

The problem is to directly compute the noise produced due to the aerodynamic interaction between a circular cylinder (rod) and an airfoil (see Fig. 3.1). The rod is placed upstream (in tandem) of the NACA 0012 airfoil. Wake/ vorticity shed from the rod convects with the flow and impinges on the downstream airfoil. This impingement (characterized oftentimes by upwash on the airfoil) produces unsteady lift on the airfoil, which then radiates as noise. At $Re_d = 48,000$, quasi-periodic vortex shedding is expected behind the rod, which gives rise to tones at the vortex shedding frequency (Strouhal number, $St \sim 0.19$) and its harmonics. In addition, the

turbulence in the vortices and the wake generate broadband noise. The resulting noise spectrum has a broadband "floor" above which tones with broadened peaks at the shedding frequency and its harmonics are observed. This problem was experimentally investigated by Jacob et al. [54] and has become a standard against which other researchers have benchmarked their code capability and accuracy. The measurements [54] include wake and boundary layer profiles (mean and turbulent statistics), near-field velocity spectra, and far-field noise.

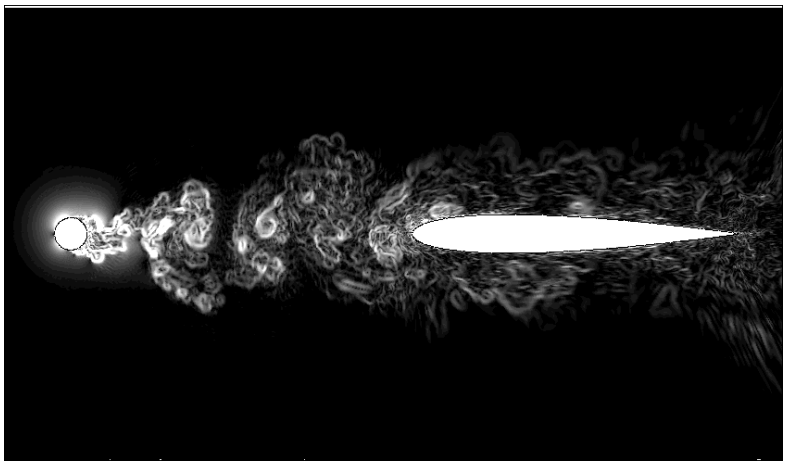

Figure 3.1: Snapshot of contours of $|\nabla\rho|^{1/4}$ to illustrate the unsteady wake of the rod interacting with the downstream airfoil.

Background

A number of numerical studies have been carried out for this specific problem. Casalino et al. [55] was the first to numerically investigate this problem using unsteady RANS simulations. The simulations were two-dimensional and the three dimensional effects on noise were modeled using a statistical model coupled with the Ffowcs Williams-Hawkings (FW-H) acoustic analogy. The statistical model was calibrated using the experimental data.

The LES technique has been used extensively to model this problem. Boudet et al. [56] reported the first LES computations for this benchmark problem. It used finite-volume, compressible LES on multi-block structured grids. Far-field noise was obtained by coupling the near-field data with a permeable FW-H solver.

Berland et al. [57] performed direct noise computations for the rod wake-airfoil interaction problem using high-order, compressible LES on overset structured grids. They also investigated the effect on noise of varying the spacing between the rod and the airfoil.

Eltaweel and Wang [58] used an incompressible LES solver coupled with a boundary element method to predict noise for this problem. An unstructured mesh composing of 22.3 million cells was used. Their results showed very good agreement with data both for near-field flow measurements as well as far-field acoustics.

Giret et al. [59, 60] used the compressible LES solver, AVBP with a fully unstructured grid to predict the aerodynamics and aeroacoustics of the rod wake-airfoil interaction problem. Far-field noise was predicted using an advanced-time formulation of the FW-H acoustic analogy [21]. They used both porous and impermeable (on the rod and airfoil surface) boundaries for evaluating the FW-H boundary integral but found little difference in the predicted noise. They also numerically investigated the effect of offsetting the airfoil in the cross-stream direction by the small amount observed in the experiments. That however did not significantly improve the agreement with the measured wake and velocity profiles.

This article presents first one-to-one comparisons between incompressible and compressible LES predictions of near-field aerodynamics and far-field acoustics for the rod-airfoil problem. The results are compared to measured data where available. The two LES solvers used are: (a) Charles, developed by Cascade Technologies, and (b) pimpleFoam from OpenFOAM. Charles solves spatially-filtered compressible Navier Stokes equations using Vreman [61] model to compute the sub-grid scale (SGS) stresses. The transient, incompressible flow solver, pimpleFoam is used with the standard Smagorinsky [62] SGS model. Both solvers use implicit spatial filtering with the filter-width set equal to the cube root of the local cell volume.

The far-field noise is computed using different approaches for the two simulations. For the Charles (compressible) simulation, data is gathered on a surface which encloses both the rod and the airfoil. The permeable surface formulation of the FW-H analogy [21] is then used to predict the farfield sound. For the pimpleFoam (incompressible) simulation, surface pressure data is extracted on the rod and the airfoil surfaces. For farfield noise computation, the LES computed surface pressure data on the airfoil is used with Amiet's formula [32], which extends

Curle's theory to predict noise from distributed dipole sources over a thin airfoil. Heretofore, this approach is loosely referred to as Amiet's theory. It should be emphasized that Amiet's formula is used in the most general sense and no approximations, e.g., thin-airfoil theory for computing lift, isotropic turbulence, etc., typically associated with Amiet's theory are made here. To the authors' knowledge, the use of Amiet's formula to predict far-field noise for this rod-airfoil configuration has not been attempted before.

Numerical Setup

Figure 3.2 shows a schematic of the problem in non-dimensional variables where length is non-dimensionalized by the airfoil chord, velocity by the speed of sound, and density by the freestream density. The rod and the airfoil are placed in tandem along the x direction, the span direction is along the z axis, and the y direction is given by the right-hand rule.

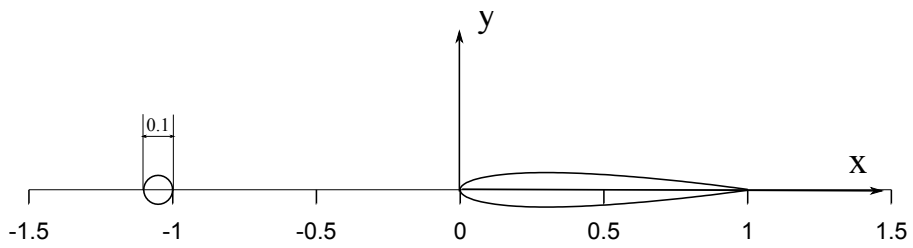

(a) 2-D Schematic

Figure 3.2: Schematic showing the non-dimensional size and positions of the rod and the airfoil.

In the experiments by Jacob et al. [54], two different rod diameters were tested. In this article, we focus on the experiment with the rod diameter, $d = 0.1 \times c$, where c is the airfoil chord. Several Reynolds numbers were tested and we limit our focus to $Re_d = 48$ K (based on d) since at that Re, broadband noise contribution is apparent in the data. The distance between the rod trailing edge and the airfoil leading edge is equal to c.

The airfoil is set at zero angle of attack in the simulations as was intended in the experiments. However, based on measured data,Jacob et al. [54] suspect that in the experiments, the airfoil might have been at a slight ($\sim 2^\circ$) angle of attack, and slightly offset in the y direction. These

geometric anomalies are not incorporated in the numerical model as a previous study [60] has shown that they have insignificant impact on the results.

Computational Mesh

Figure 3.3 shows cross-sectional views of the grid. All the grid lines are shown in the bottom halves to illustrate the grid density; fewer grid lines are shown in the upper halves to highlight the grid blocking structure. The far-field computational boundary is nearly circular with a radius of approximately $11c$. Even though the geometry is essentially 2-D (extruded in the third, spanwise dimension), the instantaneous turbulent flow over these bodies is three dimensional, and the computational domain has to be 3-D as well. However, simulating the entire spanwise length (as in the experiment) is computationally very expensive and sometimes not necessary. Periodic boundary conditions can be employed in the spanwise direction if the domain is larger than the largest eddy size along the span. Spanwise spatial coherence provides a measure of the largest eddy size and this information is used from the measured data to restrict the LES domain size to one-third of the airfoil chord in the span direction.

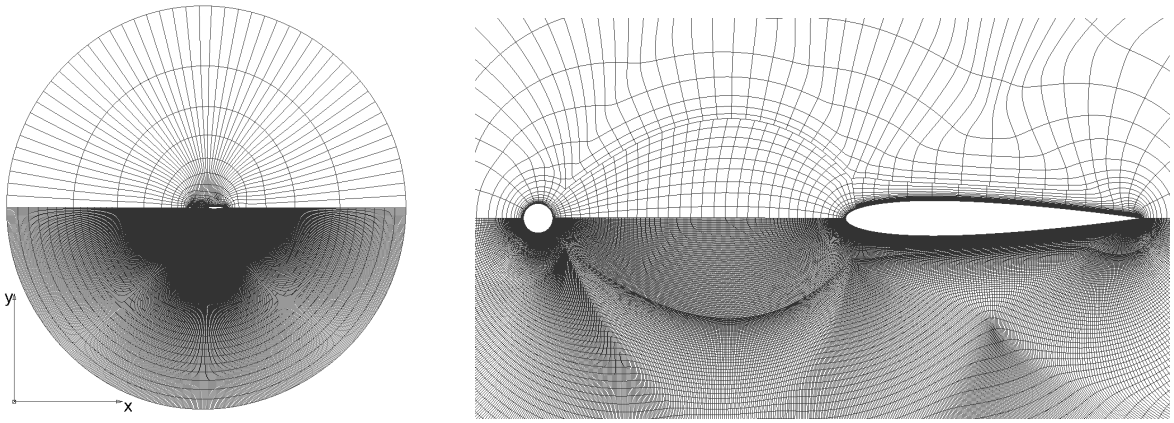

(a) Computational Domain (b) Zoomed-in view

Figure 3.3: Cross-sectional $(x-y)$ views of the computational domain and the grid around the rod and the airfoil: (a) full domain and (b) zoom view focusing on the grid near the geometries.

A fully structured grid is used for the simulations. A planar grid is first generated in the $z = 0$ plane, which is then repeated along the span to get the 3-D mesh. The planar grid is generated in three steps. The first step involves extruding the rod and the airfoil curves in the

surface normal direction. This process yields high-quality orthogonal layers of quadrilateral elements which are suitable for resolving wall boundary layers. The second step is to create quadrilateral elements between the rod and airfoil, which is crucial to capture the rod wake accurately. This is done by creating two parabolic curves, one each on the upper and lower sides, between the outer boundaries of the extruded domains. These parabolic curves are then filled with quadrilateral elements with aspect ratio of nearly 1. The final step is to create a closed curve encompassing the three domains: the rod and airfoil boundary layer regions and the wake region. This closed curve is then extruded normally until the outer radius is about $11 \times c$. This process gives a good quality mesh throughout the domain. Figure 3.3 shows the final 2-D mesh in the $z = 0$ plane. The Pointwise software (www.pointwise.com/pw) is used to generate the grid.

The blocking structure and the grid density are designed to resolve (a) the turbulence in the rod wake in the gap region, (b) the boundary layer on the rod, and (c) the boundary layer on the airfoil. The first cell height on the airfoil and the rod are chosen such that $y^+ = y/(\nu\sqrt{\rho/\tau_w}) = 1$, where ν is the fluid kinematic viscosity, τ_w is the wall shear stress, and ρ is the fluid density. This is a conservative estimate, since such small first cell height is required for resolving wall boundary layers. The problem under investigation is the interaction of the turbulence in the rod wake with the airfoil. Hence, accurate resolution of the turbulence generated in the airfoil boundary layers is not of paramount importance. This conservative approach was still taken however with the intent that in the future, the same grid could be used to study "self" (trailing edge) noise from this airfoil and a comparison could be made between "self" noise and inflow (coming from rod wake) turbulence noise.

Mesh Statistics

The total number of cells in the computational mesh is approximately 19 million. There are 5 boundary patches: rod, airfoil, two periodic and one farfield. Mesh quality metrics were evaluated using the "checkMesh" utility in OpenFOAM. The maximum cell aspect ratio is 169, the maximum mesh non-orthogonality is 30.5°, and the maximum skewness is 0.65. Both the compressible and the incompressible simulations are carried out on the same mesh.

Flow Conditions and Non-Dimensionalization

The simulations are setup in non-dimensional variables, which are denoted by the overhead tilde. The freestream values are used for non-dimensionalization. Therefore the freestream density ($\tilde{\rho}_\infty$), speed of sound ($\tilde{a}_{0_\infty}$) and temperature ($\tilde{T}_\infty$) are all unity. Using $\tilde{\rho}_\infty = 1$ and $\tilde{a}_{0_\infty} = 1$, we get $\tilde{p}_\infty = 1/\gamma = 0.7143$. The freestream velocity is obtained as $\tilde{u}_\infty = 0.2$ from $\tilde{a}_{0_\infty} = 1$ and $M_\infty = 0.2$. The length scale is normalized w.r.t. the airfoil chord length and thus the diameter of the rod in the non-dimensional units is $\tilde{d} = d/c = 0.1$. The required Reynolds number of the flow based on the rod diameter, i.e., $Re_d = 48,000$ is obtained by setting the dynamic viscosity to $\tilde{\mu} = \tilde{\rho}_\infty \tilde{u}_\infty \tilde{d}/Re_d$ equal to 4.2×10^{-7}.

In physical units, the freestream conditions are: $\rho_\infty = 1.226$ kg/m^3, $a_{0_\infty} = 360.0$ m/s (henceforth denoted by a_0), $u_\infty = 72$ m/s and $p_\infty = 113,500$ Pa. The ratios of physical units to non-dimensional units are required for direct comparisons with measurements. The ratio of dimensional to non-dimensional time is $t/\tilde{t} = u_\infty/c = 720$ s, where $c = 0.1$ m. All spectral results are plotted w.r.t. Strouhal number based on the rod diameter, $St = fd/u_\infty$.

Compressible Flow Solver, Charles

Charles solves spatially-filtered compressible Navier-Stokes equations on unstructured grids using a low dissipation, blended central-upwind scheme. The blending factor is computed locally to maximize the use of dissipation-free central scheme without sacrificing stability. Sub-grid scale (SGS) stresses are explicitly modeled with the Vreman model [61]. All flow-field variables are initialized to the freestream values. The time step used in Charles simulation is 4.0×10^{-5} in non-dimensional units.

Charles provides specific boundary conditions suitable for aeroacoustics simulations. In the annular region between the farfield boundary and a cylindrical surface of radius $8 \times c$ centered at the leading edge of the airfoil, two special features of the Charles solver are invoked: (1) the numerical scheme is switched to a dissipative upwind scheme and (2) an absorptive "sponge" layer is activated. Both these features dissipate flow perturbations away from the geometries and therefore help in reducing spurious reflections from the farfield boundaries.

Incompressible Flow Solver, pimpleFoam

The transient, incompressible flow solver, pimpleFoam is used in LES mode with the standard Smagorinsky [62] sub-grid scale model with the coefficients $C_K = 0.094$ and $C_\epsilon = 1.048$. Velocity and pressure equations are solved using the PIMPLE algorithm, which is a combination of the pressure-implicit split-operator (PISO) algorithm [63] and the semi-implicit method for pressure linked equations (SIMPLE) algorithm [64]. The PIMPLE algorithm allows the Courant Friedrichs Lewy (CFL) number to be greater than unity while still maintaining numerical stability. Time discretization is done using a second order implicit scheme and a time step of 0.005 is chosen, which is two orders of magnitude larger than that used in the Charles simulation. The flowfield is initialized with same non-dimensionalized velocity ($\tilde{u}_\infty = 0.2$), gauge pressure to zero, and kinematic viscosity is specified as $\tilde{\nu} = 4.2 \times 10^{-7}$.

Freestream boundary condition is used at the outer boundary where the velocity switches between zero gradient for outflow and fixed (prescribed) value for inflow. Pressure boundary condition is zero gradient, which fixes the flux across the boundary using freestream velocity. A second order implicit scheme is used for time marching. Gaussian integration with linear central differencing interpolation is used in computing gradients, Laplacian and divergence terms, except that divergence for the convective term is interpolated using linear upwind differencing.

Far-field Noise Prediction

Time accurate flow data in the near field is used with two different approaches to predict far-field noise: (1) the FW-H equation [21] and (2) Amiet's theory [32]. The FW-H equation requires density fluctuations in the near-field as input and hence can only be used with the compressible flow solution. Amiet's theory only requires surface pressure perturbation and hence can be used with both the incompressible and compressible solutions. In this paper, the FW-H acoustic analogy and Amiet's theory are applied to the data obtained from the Charles (compressible) and the pimpleFoam (incompressible) simulations respectively. Due to the small flow Mach number in this problem, the noise sources are primarily the unsteady forces (dipoles) on the airfoil and the rod. The contribution to far-field noise from off-surface

(quadrupole) sources has been shown by Giret et al. [60] to be significant only at very high ($St > 1$) and very low ($St < 0.05$) frequencies. Giret et al. [60] also show that quadrupole sources have little effect on the overall sound pressure level (OASPL). While Amiet's theory can only predict noise radiation due to surface (dipole) sources, the porous FW-H approach captures the contribution of the volume (quadrupole) sources that are inside the surface.

Ffowcs Williams-Hawkings Analogy

The FW-H solver used here is based on the frequency domain formulation by Lockard [65]. The frequency domain FW-H equation is

$$\begin{aligned} 4\pi\hat{p}'(\mathbf{x},\omega)H(S) = &- \iint_S i\omega\hat{Q}_n(\mathbf{x}',\omega)\, G(\mathbf{x},\mathbf{x}';\omega)\, \mathrm{d}S \\ &- \iint_S \hat{F}_i(\mathbf{x}',\omega)\, \frac{\partial G(\mathbf{x},\mathbf{x}';\omega)}{\partial x_i'}\, \mathrm{d}S \\ &- \iiint_V \hat{T}_{ij}(\mathbf{x}',\omega)H(S)\, \frac{\partial^2 G(\mathbf{x},\mathbf{x}';\omega)}{\partial x_i'\partial x_j'}\, \mathrm{d}V, \end{aligned} \tag{3.1}$$

where $H(S)$ is the Heaviside function, $\mathbf{x}'$ denotes the position of an elemental source, and $G(\mathbf{x},\mathbf{x}';\omega)$ is the three-dimensional free-space Green's function of the convected Helmholtz equation. The terms $\hat{Q}_n$, $\hat{F}_i$, and $\hat{T}_{ij}$ are Fourier transforms of Q_n, F_i, and T_{ij} respectively, where Q_n and F_i are defined using the Einstein notation as

$$Q_n = Q_i n_i = [\rho(u_i + u_{\infty,i}) - \rho_\infty u_{\infty,i}]n_i, \text{ and} \tag{3.2}$$

$$F_i = [P_{ij} + \rho(u_i - u_{\infty,i})(u_j + u_{\infty,j}) + \rho_\infty u_{\infty,i}u_{\infty,j}]n_j. \tag{3.3}$$

In the above, n_i is the unit vector normal to the integration surface, S. Fluid density (ρ), pressure (p), and velocity (u_i) are local quantities, and the compressive stress tensor, P_{ij} is defined as $P_{ij} = (p - p_\infty)\delta_{ij} - \sigma_{ij}$, where δ_{ij} is the Kronecker delta and σ_{ij} is the viscous stress tensor.

The first and second integrals on the r.h.s. of Eq. 3.1 have to be carried out over S. The integrand in the volume integral on the r.h.s. of Eq. 3.1 involves the Lighthill stress tensor, which is defined as $T_{ij} = \rho u_i u_j + P_{ij} - a_0^2(\rho - \rho_\infty)\delta_{ij}$. The volume integral is ignored in the

current formulation by assuming that all the noise sources lie within S. Solution of Eq. 3.1 yields the Fourier transform of the acoustic pressure $\hat{p}'$ at the farfield observer location, $\mathbf{x}$.

A permeable (porous) surface enclosing both the rod and the airfoil (see Fig. 3.4) is chosen for the acoustic integral evaluations. This surface incorporates ten "endcaps" [66] downstream of the airfoil to remove numerical errors due to the flux of vorticity through the surface boundaries. Time accurate flow data is sampled on this surface during the flow simulation and Eq. 3.1 is integrated using this surface data as a post processing step.

Figure 3.4: The permeable FW-H integration surface used for farfield noise prediction using the Charles simulation data. The "endcaps" remove numerical errors (expected to be uncorrelated over the end surfaces) through the integration process.

Amiet's Theory

The pressure data is collected on the airfoil surface at high sampling rate after the initial transients have been removed. Using this surface pressure data, difference in pressures, $\Delta p(x, z, t)$ between the upper and the lower surfaces of the airfoil is computed for all points (x, z) on the blade (airfoil) planform at all time, t. Note that x is along the chord and z is along the blade span. Fourier transform of $\Delta p(x, z, t)$ in time gives $\Delta\hat{p}(x, z, \omega)$, which is then used to compute the cross power spectral density, S_{QQ} between any two points, (x_1, z_1) and (x_2, z_2), using

$$S_{QQ}(x_1, x_2, z_1, z_2, \omega) = \lim_{T\to\infty} \left\{ \frac{\pi}{T} E\left[\Delta\hat{p}_T^*(x_1, z_1, \omega)\Delta\hat{p}_T(x_2, z_2, \omega)\right] \right\}. \tag{3.4}$$

In the above, $E[\ldots]$ denotes ensemble averaging operation. Further, using the idea that far-field acoustic response can be computed by assuming dipole sources in place of unsteady surface loads, Amiet gave the following expression for sound power spectral density (S_{PP}) for acoustic pressure at any given point (x, y, z) in the far-field

$$S_{PP}(x,y,z,\omega) = \left(\frac{\omega z}{4\pi a_0 \sigma^2}\right)^2 \iiint\!\!\iint S_{QQ}(x_1,x_2,\eta,\omega)\times$$
$$e^{\frac{i\omega}{a_0}\left[\beta^{-2}(x_1-x_2)(M_\infty - x/\sigma)+z\eta/\sigma\right]}\, \mathrm{d}x_1\, \mathrm{d}x_2\, \mathrm{d}z_1\, \mathrm{d}z_2, \tag{3.5}$$

where, $\eta = z_2 - z_1$, $\beta = \sqrt{1-M_\infty^2}$ and $\sigma = \sqrt{x^2+\beta^2(y^2+z^2)}$. In Eq. 3.5, S_{QQ} is taken as a function of η instead of z_1 and z_2 because only the spanwise separation between the two points (1 and 2) is relevant and not the absolute spanwise coordinates. Using the S_{QQ} computed for all point pairs, the integrals in Eq. 3.5 are numerically computed to obtain the far-field sound power spectral density, S_{PP}.

Kato's Correction

The span length of the rod-airfoil assembly simulated in our calculations is smaller than the experimental model. The predicted far-field noise therefore has to be corrected before comparing with the measured data. The correction that needs to be applied to the predicted spectra depends on spanwise coherence. If we denote spanwise coherence length by L_c and use subscripts s and e for the simulations and the experiment respectively, then Eq. 3.7 can be used for comparing the measured and the predicted spectra.

$$\begin{aligned}
\left(S_{pp}(\omega)\right)_e &= \left(S_{pp}(\omega)\right)_s + 20\log\left(L_e/L_s\right)\ \forall\ L_s < L_c,\\
\left(S_{pp}(\omega)\right)_e &= \left(S_{pp}(\omega)\right)_s + 10\log\left(L_e/L_s\right),\ \forall\ L_s > L_c,\\
\left(S_{pp}(\omega)\right)_e &= \left(S_{pp}(\omega)\right)_s + 20\log\left(L_c/L_s\right) + 10\log\left(L_e/L_c\right)\ \forall\ L_s < L_c < L_e.
\end{aligned} \tag{3.6}$$

Equation 3.7 assumes that over spanwise length L_c, there is perfect correlation which drops identically to zero outside of this region. This 'box-car' simplification by Kato and Ikegawa [67] is often used and is employed here.

The span length of the rod and airfoil assembly in the simulations (L_s) is three times the rod diameter (d), i.e., $L_s = 3d$, which is one-tenth of the span length of the model used in the experiment, i.e., $L_e = 10L_s$. Assuming that the correlation length L_c is less than L_s, the correction needed is

$$\left(S_{pp}(\omega)\right)_{s\ corr} = \left(S_{pp}(\omega)\right)_{s} + 10\log\left(L_e/L_s\right),\ \text{or,}$$
$$\left(S_{pp}(\omega)\right)_{s\ corr} = \left(S_{pp}(\omega)\right)_{s} + 10\log\left(10\right). \tag{3.7}$$

Results and Data Comparisons

The phenomena of interest in the problem under investigation are unsteady but statistically stationary. The interest is not in transient phenomena such as instantaneous/impulsive start of the rod/airfoil combination. In the experiments, the wind tunnel is started and the rig is allowed to reach a statistically stationary state before measurements are taken. Similarly, the computations have to reach a statistically stationary state before any unsteady data can be gathered from the simulations. Removal of initial transients from the computational domain is therefore required before meaningful results can be sampled. The time period of wake shedding from the cylinder for $Re_d = 48,000$ is approximately 2.63 non-dimensional time units. The data collection was started after 40 time units and then sampled for approximately 45 shedding periods (approximately 118 time units) in both the simulations. This data is used for statistical analysis presented in the following sections.

The experimentally measured data includes mean and r.m.s. velocity profiles at various locations ahead of and behind the airfoil, near-field velocity spectra, as well as far-field acoustic spectra and directivity. Comparisons against these measurements are systematically presented in this section. Code-to-code comparisons of some other relevant quantities that were not measured are also presented. Figure 3.5 shows the contours of $|\nabla p|^{1/4}$ as computed from the Charles simulation. The fourth root is taken only to enhance the contrast in the contours. The acoustic radiation away from the geometries can be clearly seen in this compressible calculation.

Surface Pressure

The pressure distributions on the rod and airfoil surfaces are obtained by averaging the time-accurate data (sampled over 45 shedding periods) in time as well as in space (along the span direction). The mean pressure coefficient, $\bar{C}_P$ and root mean squared pressure coefficient,

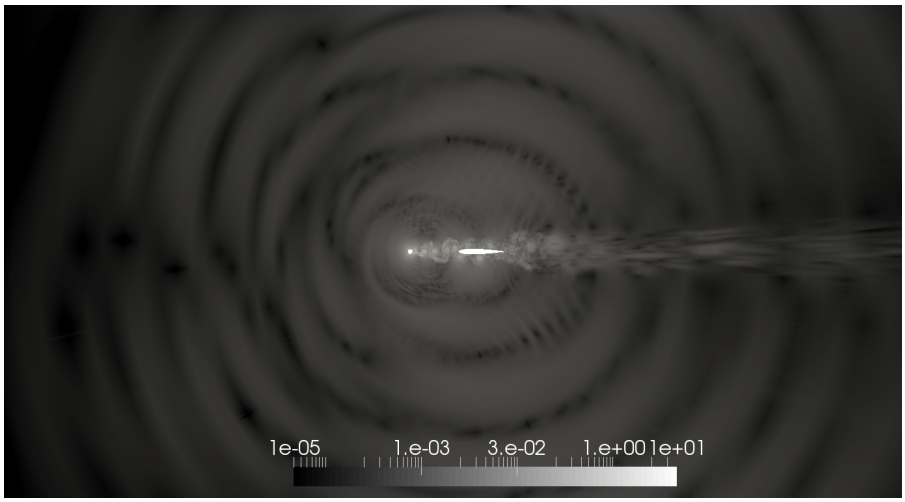

Figure 3.5: Contours of $|\nabla p|^{1/4}$ from Charles simulation.

$C_{P,rms}$ using this averaging procedure are compared between the two predictions, and against data where available, in Figs. 3.6 and 3.9. The pressure coefficients on the rod are plotted w.r.t. the angle measured from upstream. Thus, 0° and 180° denote the rod leading and trailing stagnation points respectively. For the airfoil, the pressure coefficients are plotted along the chord line.

Figure 3.6 (a) shows that the expected value of 1 is obtained for $\bar{C}_P$ at the rod leading stagnation point after which $\bar{C}_P$ drops steadily until the peak negative value is reached at 70°. Both the solvers predict the same peak location, which matches with the experimental data from Norberg [7]. Two sets of data from Norberg [7] are shown which correspond to Re_d of 20,000 and 60,000. The agreement between pimpleFoam prediction with data is very good; the Charles solution shows a higher drop in $\bar{C}_P$.

Figure 3.6 (b) shows that $C_{P,rms}$ starts from zero at the rod leading edge and then monotonically increases with the angular location until 80°, after which it drops rapidly. The flow separates approximately between $75° - 80°$ as observed by Achenbach [68]. Both solvers predict the same peak location for $C_{P,rms}$ but the magnitudes differ, with Charles predicting higher fluctuations near the surface.

The predicted boundary layer velocity profiles on the rod surface are compared in Fig. 3.7 to investigate the differences in $\bar{C}_P$ and $C_{P,rms}$ profiles for the two solvers. The boundary layer

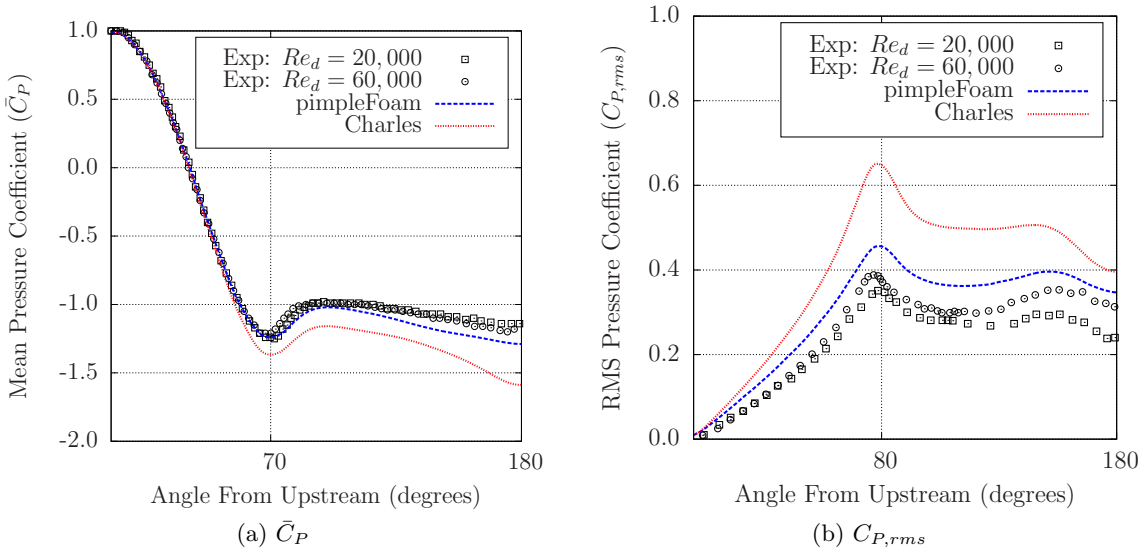

(a) $\bar{C}_P$ (b) $C_{P,rms}$

Figure 3.6: Mean and r.m.s. aerodynamic pressure coefficients on the rod. Experimental data in these plots is from Norberg [7].

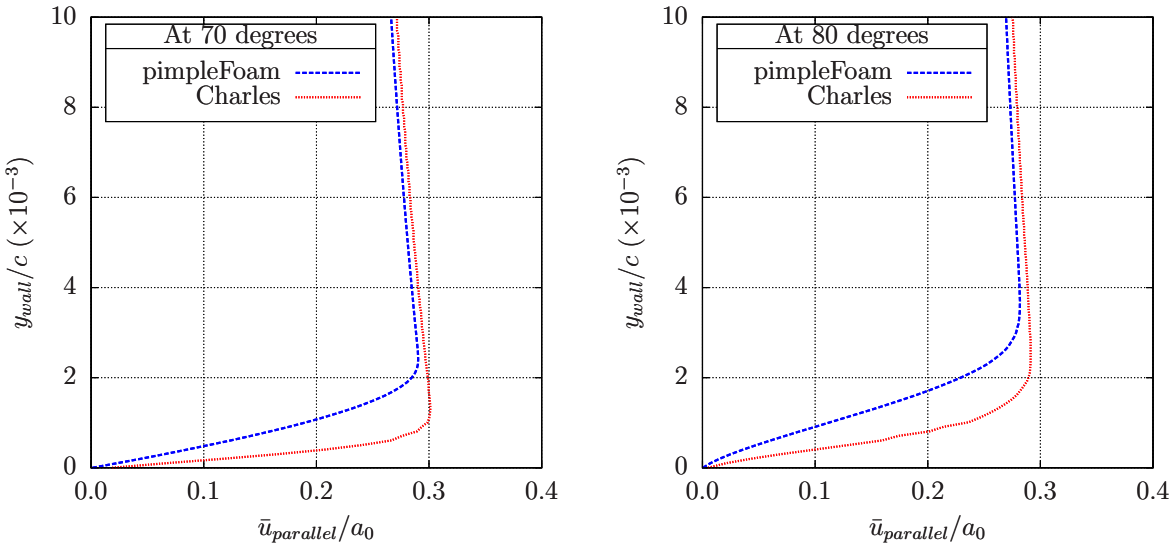

Figure 3.7: Wall parallel velocity profiles w.r.t. normal distance from surface on the rod at angular locations 70° and 80°.

profiles are compared at the angular locations 70° and 80°, corresponding to the peak locations of $\bar{C}_P$ and $C_{P,rms}$ respectively. The boundary layer thickness predicted by pimpleFoam is almost twice that from the Charles simulation. Also, the wall-normal gradient of the velocity predicted by Charles is higher than that for pimpleFoam, implying a higher skin friction coefficient in the Charles simulation. This indicates that the Charles simulation has higher turbulence intensity near the surface, which is consistent with the higher $C_{P,rms}$ prediction in Fig. 3.6 (b).

There are two potential reasons for these differences between the solvers: (1) the numerical scheme in Charles is less dissipative than pimpleFoam, and (2) the standard Smagorinsky SGS model used in pimpleFoam is known to be less accurate than the Vreman model used in Charles. Despite that, the pimpleFoam predictions of $\bar{C}_P$ and $C_{P,rms}$ seem to compare better with data. Figure 3.8 compares snapshots of the predicted SGS eddy viscosity, ν_{SGS} between the two solvers. A more diffused ν_{SGS} is seen in the pimpleFoam simulation, while the Charles simulation shows a much more localized use of the SGS stresses. With the current simulations it is difficult to identify if the discrepancies in predictions are due to the differences in the numerical schemes or the SGS models. Both numerical diffusion and eddy viscosity act as sinks in the momentum equation, and due to the implicit spatial filtering employed, it is difficult to separate the contributions from the two.

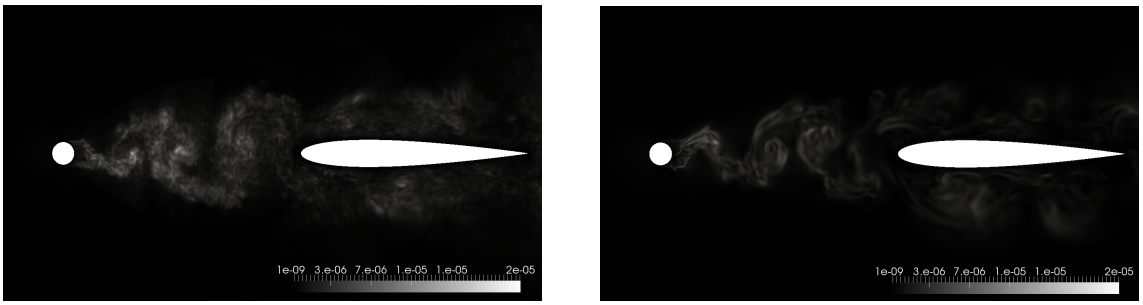

(a) Charles (b) pimpleFoam

Figure 3.8: Instantenous turbulent eddy viscosity, ν_{SGS} from the two simulations.

Mean and r.m.s. pressure coefficients are also compared on the airfoil surface. Figure 3.9 (a) compares the predicted $\bar{C}_P$ distributions on the airfoil which peak near $x/c \sim 0.2$ in both simulations. Figure 3.9 (b) compares the predicted $C_{P,rms}$ distributions. The relatively

large $C_{P,rms}$ near the leading edge indicates that unsteady lift, which is the primary source of interaction noise from the airfoil, is concentrated near the leading edge. The unsteady lift of the airfoil is determined by the fluctuating 'upwash' on the airfoil induced by the rod wake. The rod wake (and thus the upwash) has a dominant frequency given by $St \sim 0.19$. This corresponds to a reduced frequency of 1.0 based on the airfoil semi chord. The unsteady lift concentration at the leading edge is expected at this reduced frequency from the thin airfoil theory.

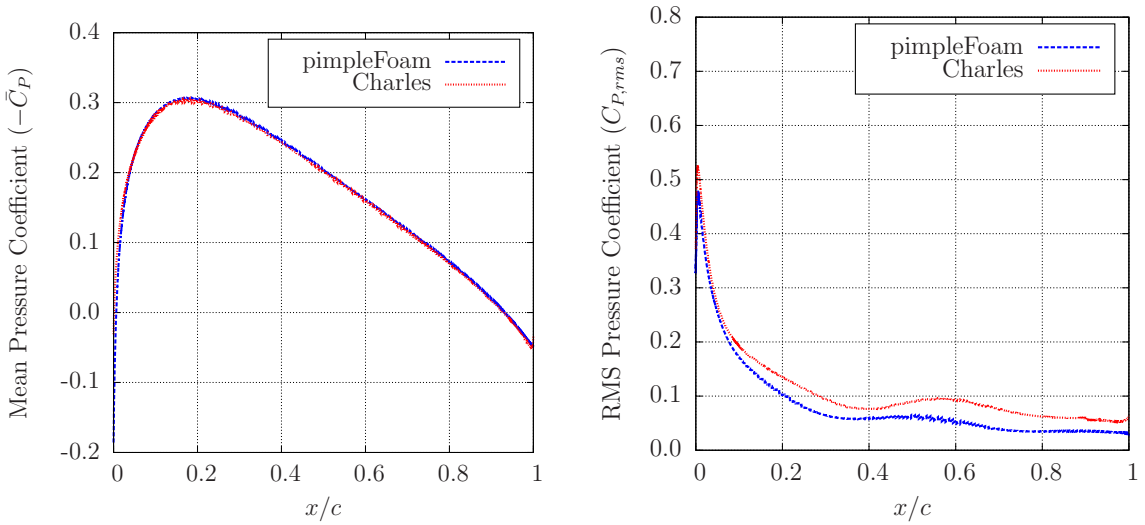

(a) $\bar{C}_P$ (b) $C_{P,rms}$

Figure 3.9: Mean and r.m.s. aerodynamic pressure coefficients on the airfoil.

Meanflow and RMS Velocity Comparisons

The predicted mean and the r.m.s. velocity profiles are obtained at various axial locations (stations) as well as the centerline between the rod and the airfoil from both simulations. The axial stations are specified in terms of non-dimensional distance along the x axis. Figure 3.10 shows the locations of these axial stations as well as the centerline (marked as CL in the figure).

Figure 3.11 compares the two predictions of the mean and r.m.s. axial velocities, $\bar{\tilde{u}}$ and $\tilde{u}_{rms}$ respectively, along the centerline. As mentioned earlier, the differences in the numerical schemes and the SGS models are responsible for the code-to-code differences in u_{rms} predictions.

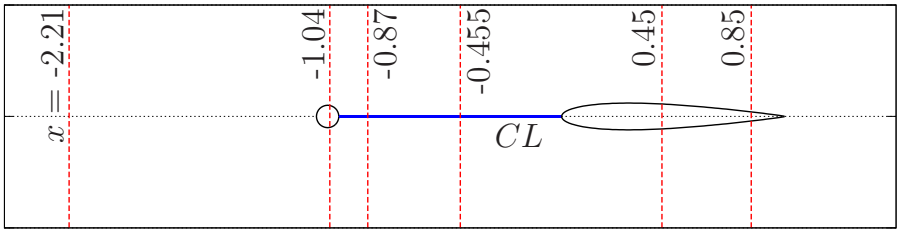

Figure 3.10: Axial locations and centerline (CL) where mean and r.m.s. wake/ velocity comparisons are made.

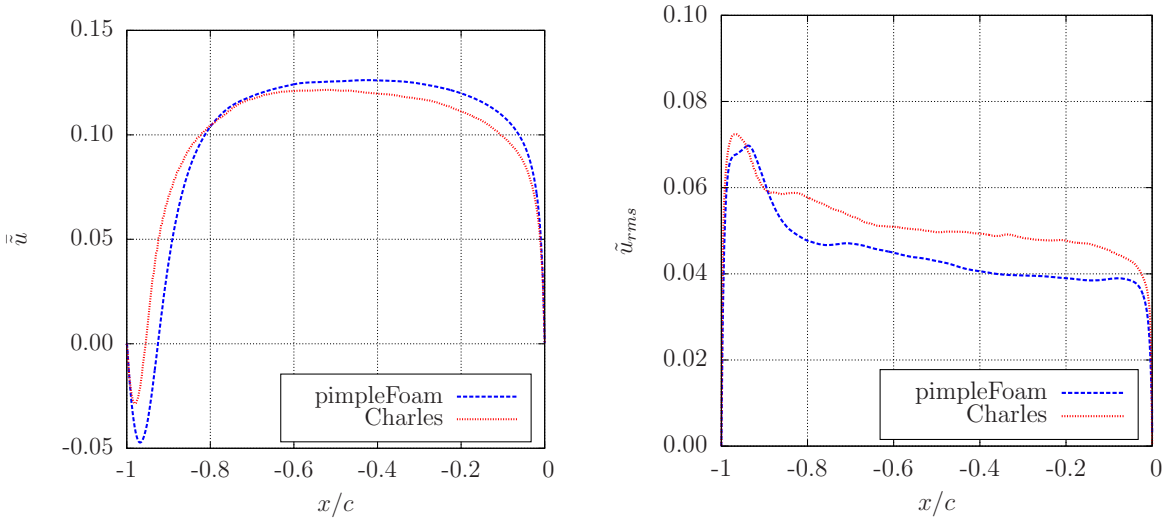

(a) Mean velocity

(b) RMS velocity

Figure 3.11: Predicted mean and r.m.s. axial velocity along the centerline.

The measurements of $\bar{\tilde{u}}$ and $\tilde{u}_{rms}$ profiles from Jacob et al. [54] are compared with the predictions at the axial stations marked in Fig. 3.10. These comparisons are plotted in Fig. 3.12. The reader should bear in mind two key differences between the experiment and the simulations when comparing the results against the measurements: (1) in the experiment, the airfoil is slightly offset in the positive y direction by a distance of about 2% chord, and (2) the airfoil is at a slight angle-of-attack (around 2^o). These make the measured profiles slightly asymmetric, whereas the predicted time-averaged profiles are symmetric.

Figure 3.12 (a and b) shows the $\bar{\tilde{u}}$ and $\tilde{u}_{rms}$ upstream of the rod (essentially showing the freestream conditions). The data shows a very slight inflow turbulence intensity, which is identically zero in the simulations. Figure 3.12 (c and d) plots the velocity profiles on the rod

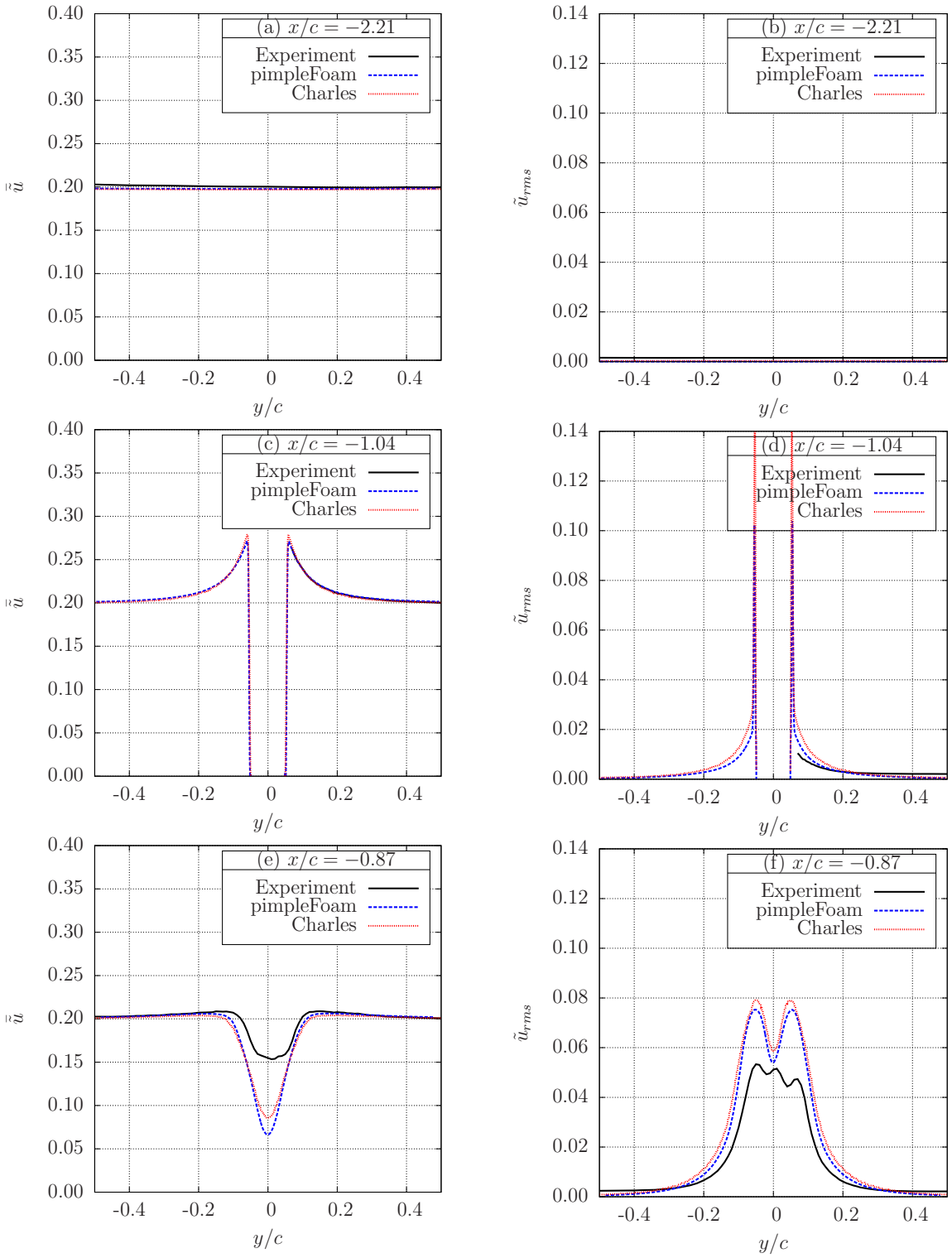

Figure 3.12: Mean and r.m.s. velocity comparisons between data and predictions.

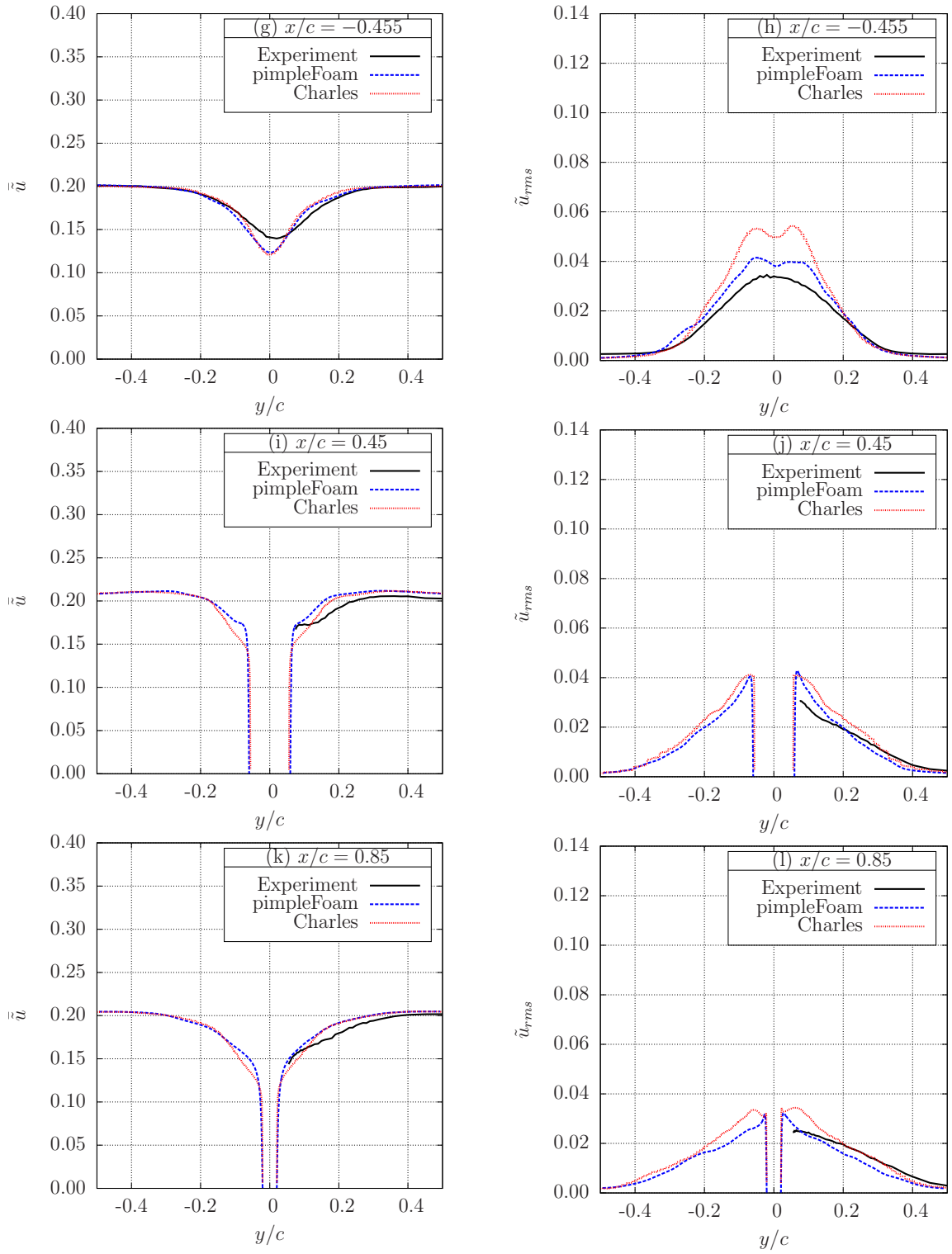

Figure 3.12: (Continued) Mean and r.m.s. velocity comparisons between data and predictions.

past the maximum thickness point. The data was only collected above the rod (positive y) in the experiment. Flow acceleration due to rod thickness, and the development of the boundary layer (as seen in the $\tilde{u}_{rms}$ profiles) are captured by both solvers. Also, both $\bar{\tilde{u}}$ and $\tilde{u}_{rms}$ drop to zero at y/c of the points on the rod surface, satisfying the no-slip boundary condition.

Figure 3.12 (e, f, g and h) shows the profiles between the rod and the airfoil at $x/c = -0.87$ and $x/c = -0.255$. A large discrepancy in the mean velocity is observed in Fig. 3.12 (e) and the authors suspect the measured data at this station. The peak velocity deficit in the wake is expected to reduce with distance away from the rod. This is observed in the simulations, however the measured mean velocity profiles in Fig. 3.12 (e and g) shows the peak velocity deficit increasing with downstream distance. Some discrepancy however can be attributed to numerics as well - the simulations consistently over-predict the $\tilde{u}_{rms}$ (a measure of turbulence intensity). Figure 3.12 (g) reflects the slight asymmetry in the experiments; the peak velocity deficit appears to be at a slightly positive value of y/c. Jacob et al. [54] assert that this slight asymmetry does not affect the far-field noise and hence no attempt was made to correct for this anomaly.

Velocity profiles in Fig. 3.12 (i, j, k and l) were measured only on one side of the airfoil (positive y). The velocity profiles on the airfoil are determined by the rod wake turbulence (due to the high intensity and length scale) rather than the development of the airfoil boundary layer. Hence the errors accumulated in the simulations upstream of the airfoil persist in these comparisons.

In general the mean velocity deficit and r.m.s. velocity predicted by the two solvers are in good agreement. Both however over-predict the mean velocity deficit and the r.m.s. velocity in the wake.

Spectral Comparisons in the Near Field

While comparing the mean and r.m.s. velocity profiles helps in assessing flow prediction accuracy, the interest is in predicting radiated noise, which has its sources in the turbulence spectra. Velocity and pressure spectra on the surface, and in the near field of the rod and the airfoil are analyzed in this section.

Velocity Spectra

Measurements are available of near-field power spectral density (PSD) of velocity at a few locations close to the rod and the airfoil geometries. PSD and other related quantities are defined in A. The near-field velocity spectra are compared against the data measured at two locations. These are marked as "A" and "B" in Fig. 3.13.

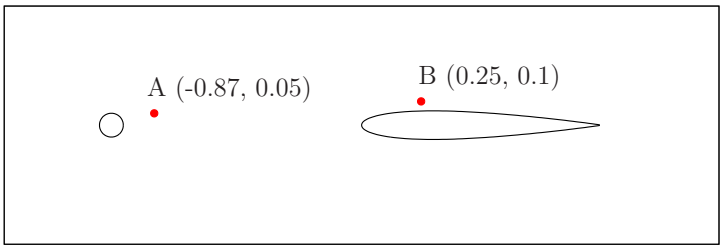

Figure 3.13: Locations denoted by "A" and "B" at which near-field spectral comparisons are made.

Instantaneous velocity data was gathered for both simulations at points "A" and "B" for 45 periods of wake shedding. The spectra was computed at all spanwise locations and averaged to obtain the final velocity spectra at these two points. Figure 3.14 shows the axial velocity power spectral density comparisons at points "A" and "B". Two essential features of the measured spectra - (1) the spectral peak amplitude at $St \sim 0.19$, and (2) the decay beyond the spectral peak, are captured well by the predictions. In Fig. 3.14 and all subsequent spectra plots, this wake shedding frequency ($St \sim 0.19$) is denoted by f_1 and its second, third, and fourth harmonics by f_2, f_3 and f_4 respectively. The Strouhal numbers corresponding to f_1, f_2, f_3, and f_4 are 0.19, 0.38, 0.57 and 0.76 respectively.

Figure 3.14 (a) shows that the agreement between data and predictions is quite good, especially for pimpleFoam predictions. Charles slightly underpredicts the broadband spectra at point "A". Both solvers predict the second and the third harmonics (f_1 and f_2) at point "A". These higher harmonics are not as prominent in the data as well as the simulations at point "B". This is due to the wake structure disintegrating into turbulence as it evolves downstream. Both plots also show that the predicted spectra from pimpleFoam fall (with frequency) more rapidly than Charles at very high frequencies.

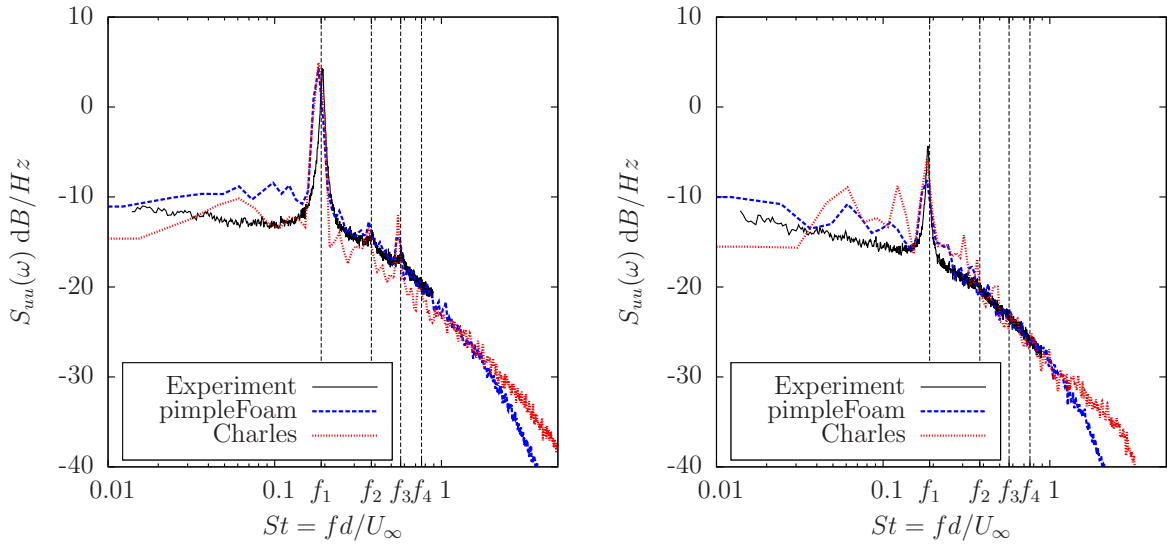

(a) Spectra at point "A"

(b) Spectra at point "B"

Figure 3.14: Predicted velocity power spectral density, $S_{uu}(\omega)$ dB/Hz, at points "A" and "B" from Fig. 3.13.

Pressure Spectra

The pressure power spectral densities (PSDs) are also obtained from the simulations at points "A" and "B" in the same manner as the velocity PSDs. Figure 3.15 compares the pressure PSDs predicted by the two solvers. The spectrum at point "A" shows two prominent peaks at f_1 and f_2 and a faint but discernible peak at f_3. The spectrum at point "B" only shows one prominent peak at f_1. The peak at the second harmonic (f_2) at point "A" is much more prominent in the pressure spectra than the velocity spectra. f_1 is the frequency at which vortices are shed from one side (say the upper half) of the rod. The point "A" is offset in the positive y direction from the centerline. Its location is such that it is in the path of the vorticity shed from the upper half of the rod but not the lower half. Therefore, in the spectra of a convected field variable such as velocity, the fundamental (dominant) frequency is expected to be f_1 at this point. The hydrodynamic pressure field at this point however is influenced by the vortices shed from both the top and bottom halves and hence will have higher energy in f_2.

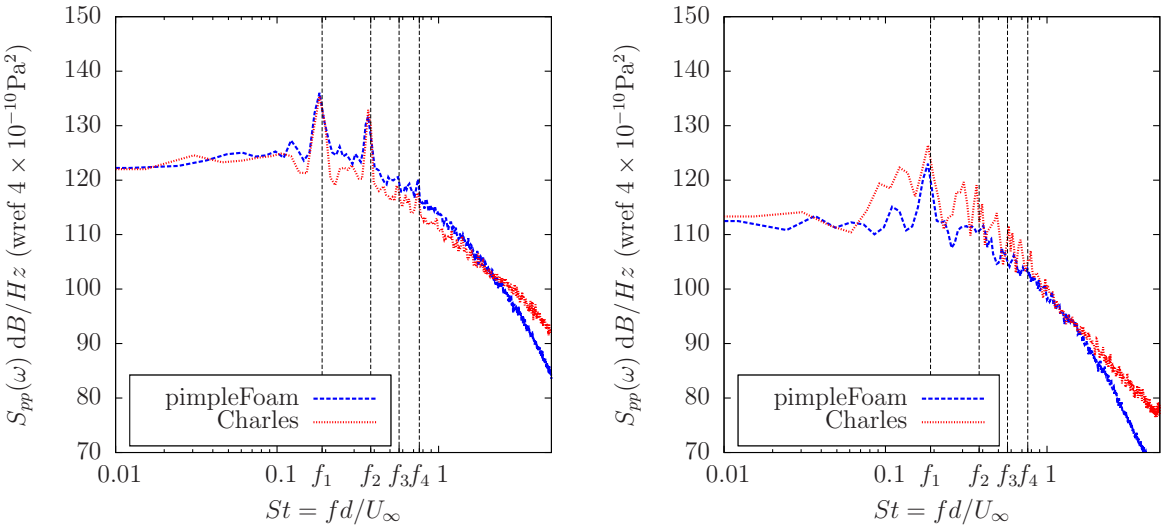

(a) Spectra at point "A"

(b) Spectra at point "B"

Figure 3.15: Predicted pressure PSD at points A$(-0.87c, 0.05c)$ and B$(0.25c, 0.1c)$.

The point "B" is located above the airfoil. Due to the exact alignment of the rod-wake centerline with the flow velocity, the vortices shed from the upper half of the rod go above the airfoil while the vortices shed from the lower half go below the airfoil. The point "B" therefore experience excitation at the fundamental frequency of f_1. The solid surfaces of the airfoil can withstand pressure differences and hence even the pressure field from the vortices below the airfoil have much reduced influence on the pressure at "B". Therefore there is no clear peak at f_2 in the predicted pressure spectra at "B".

Surface Pressure Spectra

The pressure data is also collected on the entire surfaces of both geometries (rod and airfoil) at high sampling frequency and the pressure PSD is computed and averaged over the span. Figure 3.16 and 3.17 show the pressure PSDs for both simulations on the rod and the airfoil surfaces respectively.

In the pressure PSD on the rod surface (Fig. 3.16) the abscissa and the ordinate represent the angular location and the Strouhal number respectively. The magnitude of the pressure PSD is shown with contours. Figure 3.16 shows a band at $St \sim 0.19$, corresponding to the peak shedding frequency, which spans all the angular locations except near the leading and trailing

stagnation points of the rod. These contours show another band of high PSD magnitude at $St \sim 0.38$ centered at 180° and spanning roughly 60°. At angular locations close to 180°, the influence of vortex shedding from both the upper and lower halves of the rod is felt equally, and hence the fundamental frequency is expected to be f_2 ($St \sim 0.38$). This corresponds to the fluctuating drag force on the rod.

Figure 3.17 shows the PSD contours on the upper ($y > 0$) airfoil surface where the abscissa now represents the location along the chord. These plots show high levels of PSD magnitude for all Strouhal numbers near the leading edge and a band of high level at $St \sim 0.19$ for most of the airfoil.

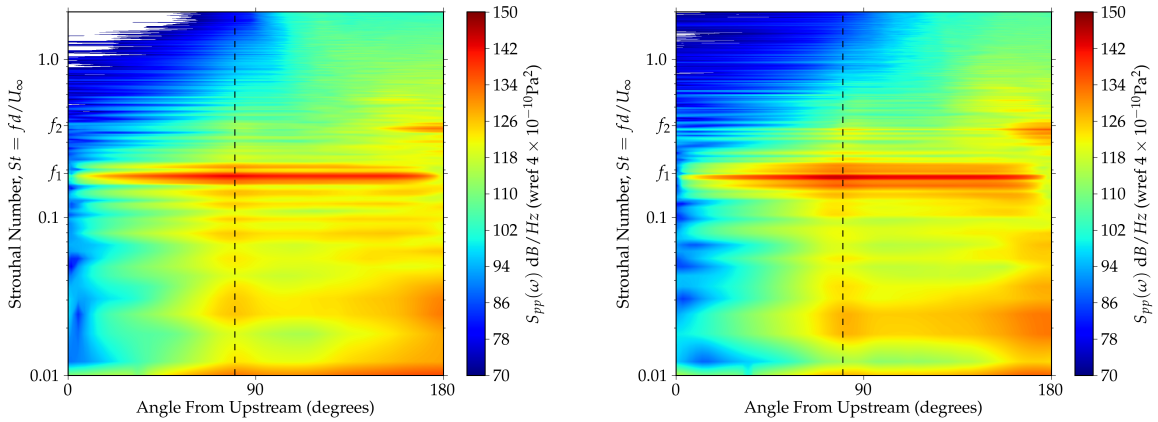

(a) pimpleFoam (b) Charles

Figure 3.16: Predicted pressure PSD on the rod surface for both solvers.

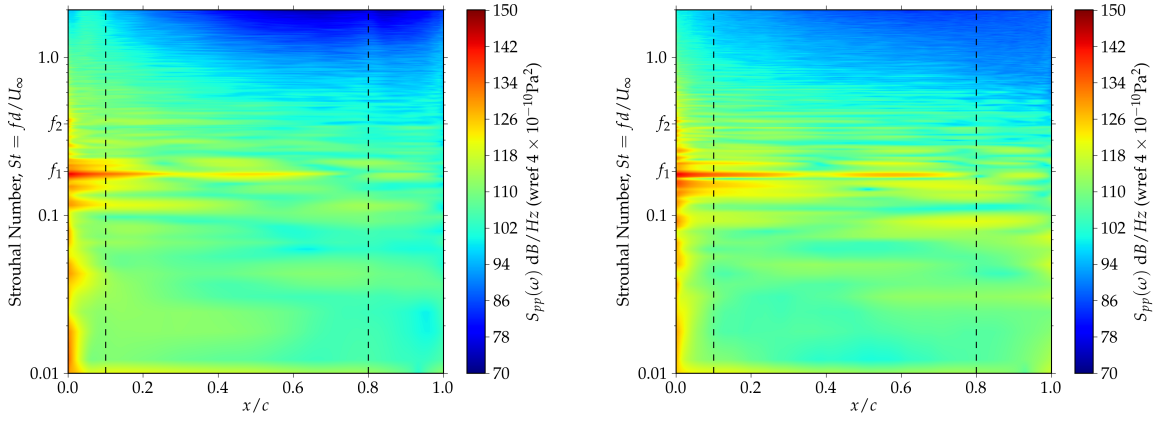

(a) pimpleFoam (b) Charles

Figure 3.17: Predicted pressure PSD on the upper surface of the airfoil for both solvers.

While the contour plots give a largely qualitative overall picture, the pressure PSDs at a selected few points on the geometries are examined in detail here. Figure 3.18 compares the pressure PSDs at three locations on the rod: at the leading and trailing stagnation points, and where the r.m.s. pressure peaks. These correspond to angular locations of 0°, 180°, and 80° respectively (see Fig. 3.6). The spectra at the rod leading edge have very low energy but they do exhibit peaks at the first and the second harmonics. This is really the hydrodynamic pressure field that is setup further downstream on the rod surface and in the wake. The PSDs at 80° and 180° show peaks at f_1 and f_2 respectively. This is due to the alternate vortex shedding from the top and bottom halves of the rod. The Charles prediction show a large spectral broadening (haystacking) near f_2 suggesting that the wake structure is more turbulent. There is also a discernible peak at f_2 in the Charles prediction of pressure PSD at 80° (see Fig. 3.18 (b)), which is not seen in the pimpleFoam simulation. This could potentially be due to the near-field acoustic (pressure) waves in the compressible flow solution.

Figure 3.19 compares the pressure PSDs at three locations on the airfoil upper surface defined by $x/c = 0, 0.1$ and 0.8. The predictions from both the solvers are very similar. The pimpleFoam prediction of the pressure PSD at the leading edge shows a discernible peak at f_2. Due to the geometric symmetry the leading edge is impacted by the vortices shed from both upper and lower sides of the rod and therefore there is no peak in the spectra at f_1. In the Charles simulation the peak at f_2 is not distinct; it is unclear if there are multiple peaks or just statistical scatter due to insufficient sampling. The predicted PSDs at $x/c = 0.1$ on the upper airfoil surface have a peak at the first harmonic as only the vortices shed from the upper half of the rod impact that point directly. The coherent vortices in the rod wake disintegrate into turbulence as they convect down the airfoil. The predicted PSDs at $x/c = 0.8$ therefore do not reveal any peaks.

Sectional Lift and Drag Spectra

Power spectral densities are also computed for the integrated sectional lift and drag coefficients on the rod and airfoil geometries. The spectra are averaged in the spanwise direction to reduce statistical scatter.

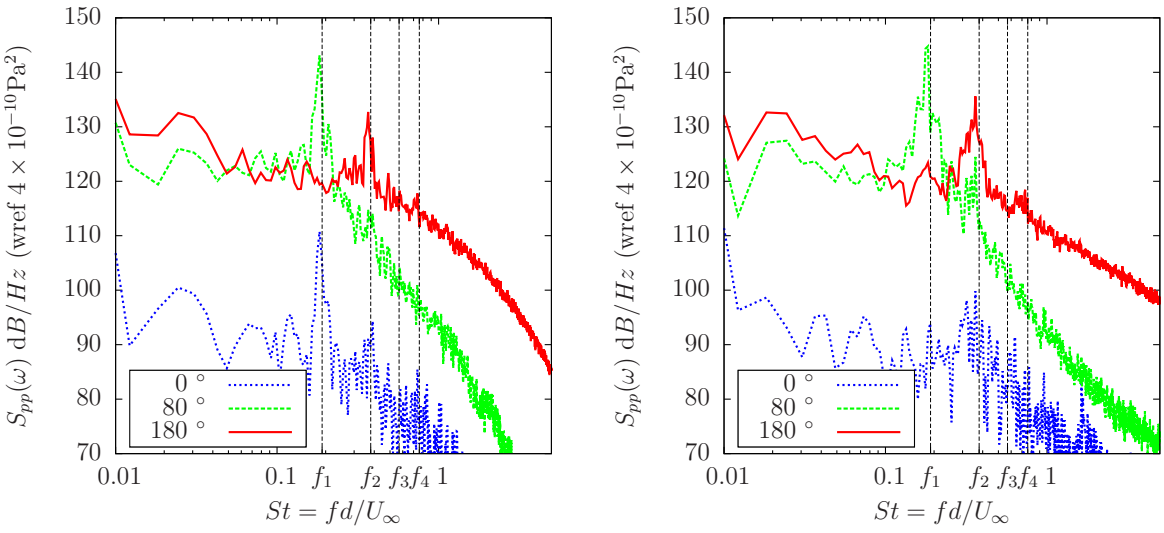

(a) pimpleFoam (b) Charles

Figure 3.18: Predicted pressure PSD at three angular locations on the rod surface for both solvers.

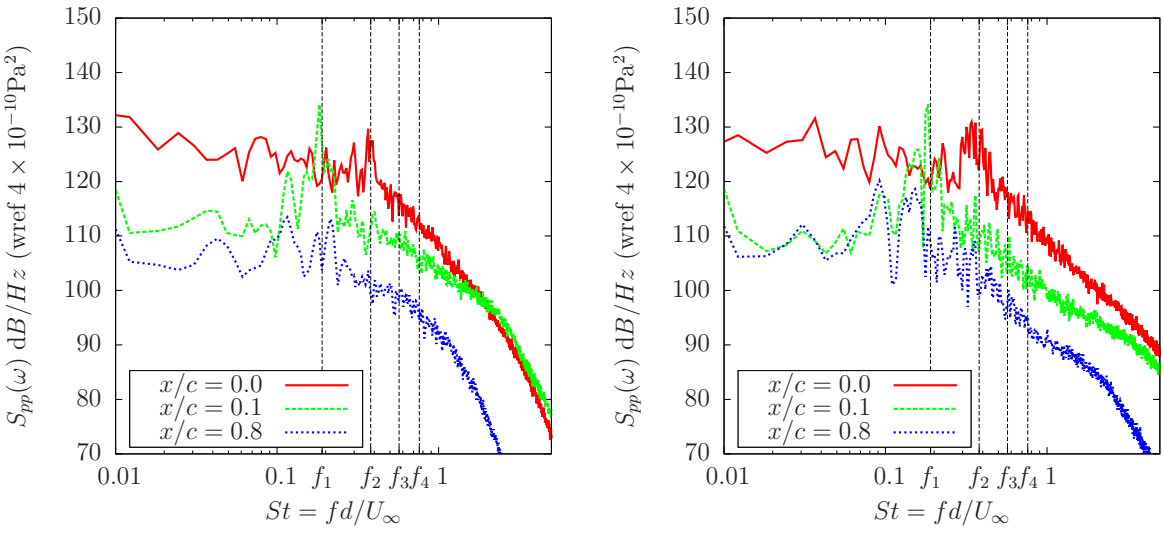

(a) pimpleFoam (b) Charles

Figure 3.19: Predicted pressure PSD at three chordwise locations on the upper surface of the airfoil for both solvers.

Figure 3.20 compares the lift PSD for the rod and the airfoil for both solvers. Both predictions for the rod PSD spectra show peaks at f_1 and f_3, but no peak at f_2. The f_1 frequency ($St \sim 0.19$) corresponds to one wake shedding cycle which involves two vortices shed alternately from the upper and lower halves of the rod. While all higher harmonics are possible, the odd harmonics, i.e., $f_3 = 3 \times f_1$, $f_5 = 5 \times f_1$, etc. are more plausible because of the alternate vortex shedding.

Figure 3.21 compares the sectional drag PSDs, which shows peaks at f_2 but not at f_1. The drag on the rod is dominated by pressure. Due to the geometric and aerodynamic symmetry about $y = 0$ plane, the contribution to sectional drag (a surface integral quantity) due to the vortices shed from both sides of the rod is statistically identical. Therefore, the sectional drag has a fundamental frequency of $f_2 = 2 \times f_1$. The higher harmonics f_4, f_6 etc. are probably present but very small in magnitude and hence cannot be differentiated from the broadband floor.

Spatial Coherence

Spatial coherence γ^2, as defined in A, is computed on the airfoil surface at the maximum thickness location. The span length of the model in the simulations is $0.3 \times c$. Due to the use of periodic boundary condition, spatial coherence can be computed for half that length i.e., $0.15 \times c$. Figure 3.22 shows the computed γ^2 for f_1, f_2, f_3, and f_4. Per expectations, the coherence over half span reduced with increasing frequency. Based on these results, the flow over the airfoil can be assumed to be decorrelated over the simulated span for $St > 0.38$. The spatial coherence at $St = 0.19$ over half-span is a little high and that can lead to some errors in correcting the noise prediction for span length differences between the experiment and the simulations.

Far-field Spectra

Figure 3.23 compares the predicted (with span-length correction) far-field acoustic pressure PSD against the data measured at a point directly above the airfoil leading edge at a distance of $18.5 \times c$. The predictions are made using the FW-H method with the Charles data, and

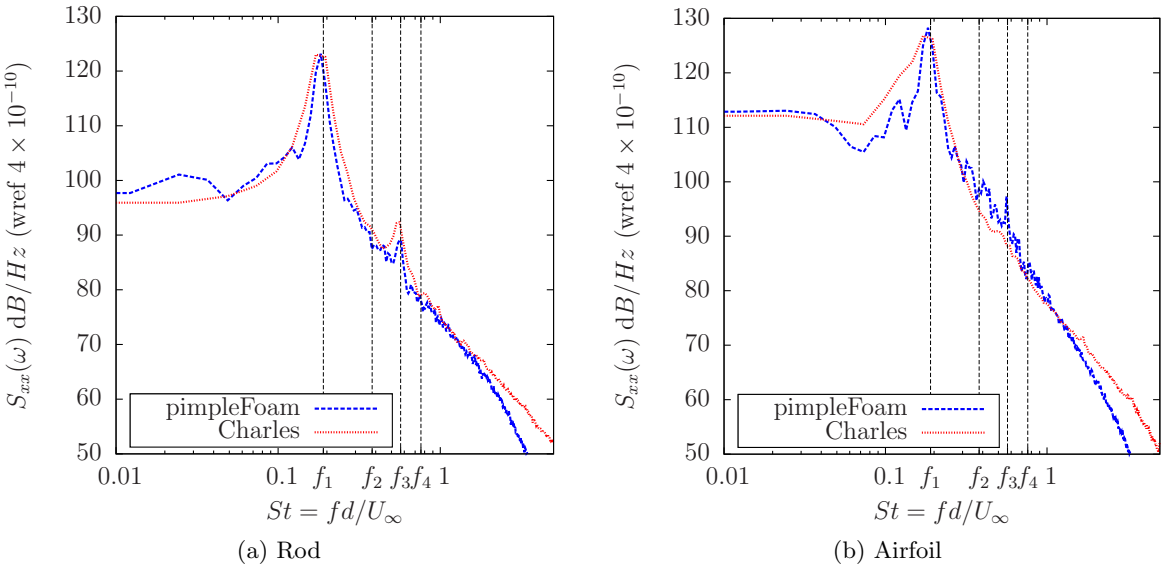

(a) Rod (b) Airfoil

Figure 3.20: Predicted PSDs of sectional lift on the rod and the airfoil for both solvers.

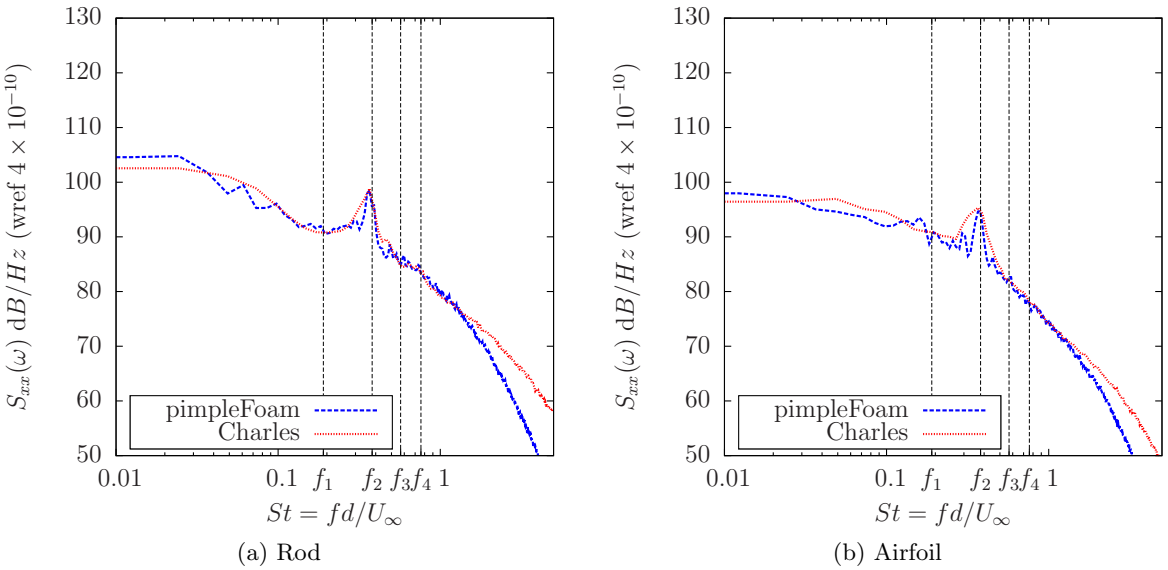

(a) Rod (b) Airfoil

Figure 3.21: Predicted PSDs of sectional drag on the rod and the airfoil for both solvers.

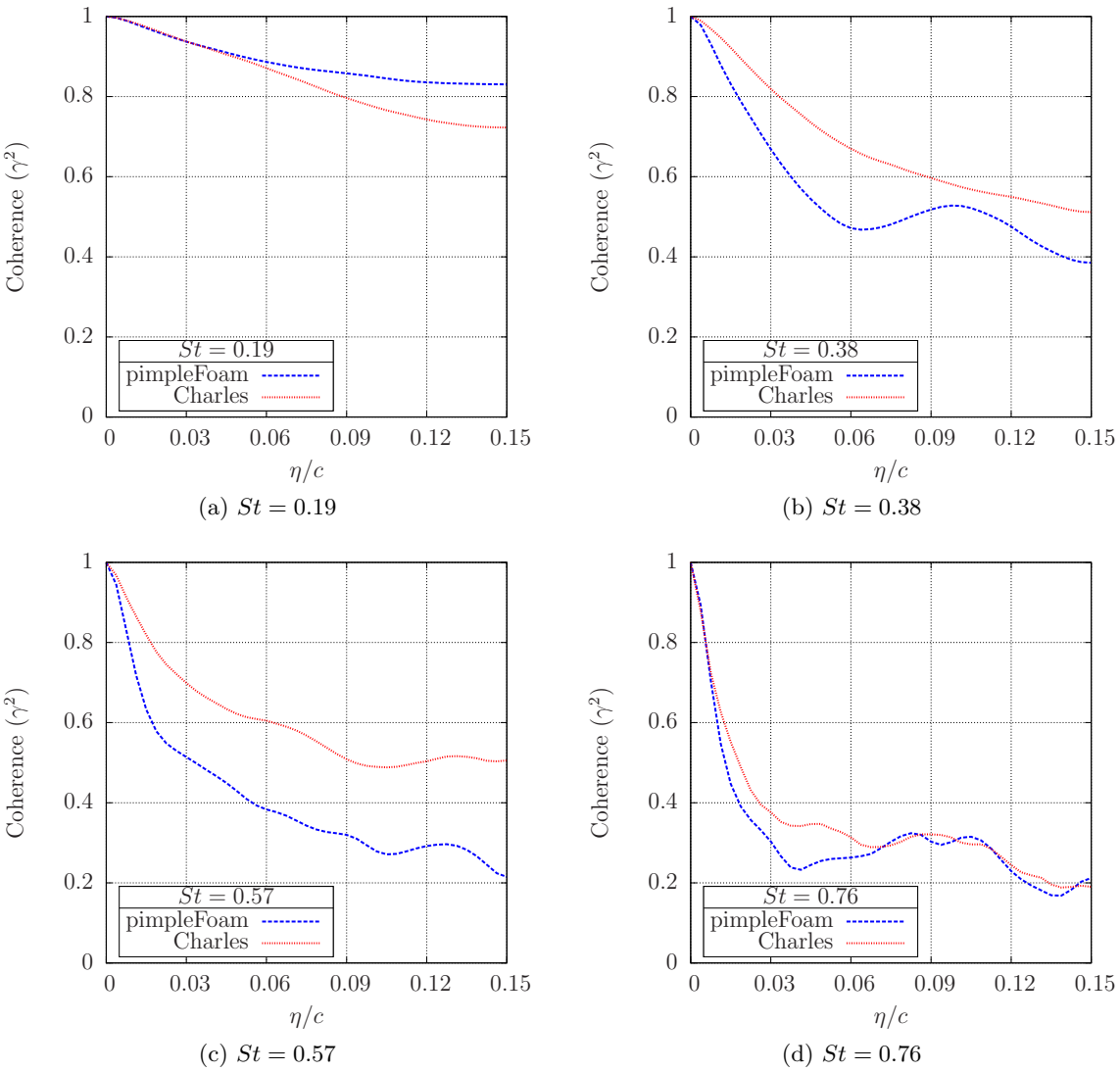

(a) $St = 0.19$ (b) $St = 0.38$

(c) $St = 0.57$ (d) $St = 0.76$

Figure 3.22: Predicted spanwise spatial pressure coherence on the airfoil at the max thickness location at four different Strouhal numbers.

Amiet's theory using pimpleFoam simulation data. The agreement between the measured and the predicted spectra in Fig. 3.23 is good; FW-H method seem to slightly overpredict the noise at high frequencies, whereas Amiet's theory seem to slightly underpredict the noise at high frequencies. The latter could be due to pimpleFoam not resolving enough turbulence scales as compared to Charles, this is seen earlier in all spectral plots. The spectral peak at wake shedding frequency (f_1) and the spectral fall-off are reasonably well captured.The predictions in Fig. 3.23 are averaged over multiple samples to reduce the statistical scatter in the predicted spectra.

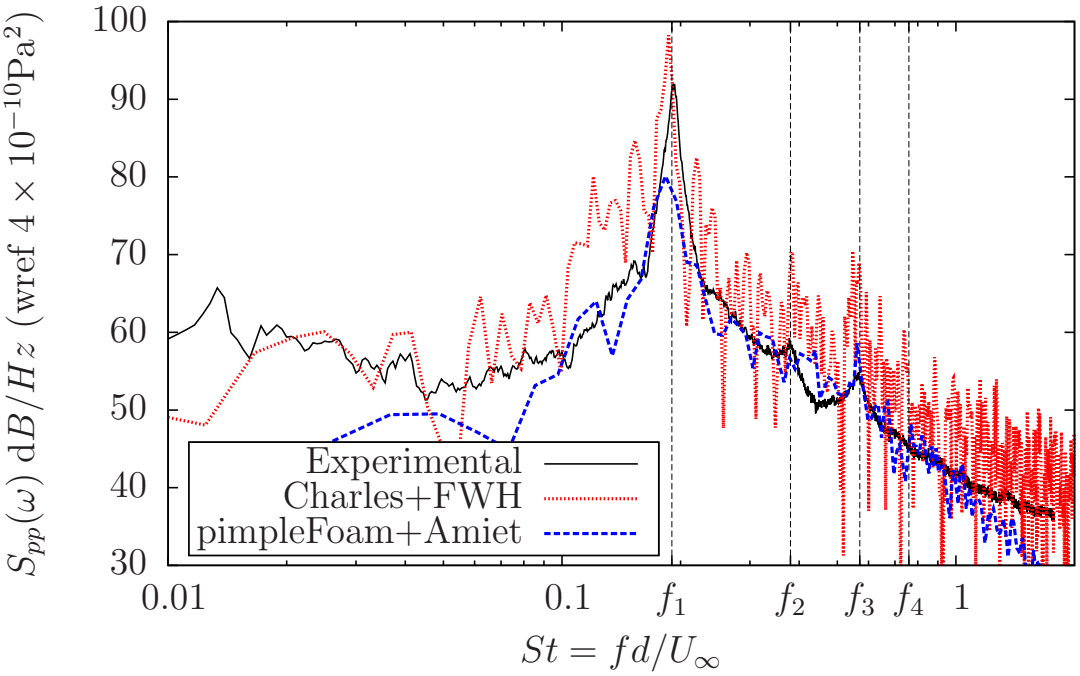

Figure 3.23: Far-field pressure spectral density (PSD) directly above the airfoil leading edge ($\theta = 90^0$) at a distance of 18.5 chords. Predictions using the FW-H method and Amiet's theory are compared with measured data.

Predicted and measured directivities of the peak noise frequency ($f_1, St \sim 0.19$) are compared in Fig. 3.24. The angles shown on the periphery of the plot are measured from downstream. In making the comparison, the measured data (microphone angles) has been corrected (using Amiet's correction) for refraction due to the shear layer present in the experiment. The overall shape is captured by the simulations. The dip in FW-H predictions with compressible flow input is due to out-of-phase interference between noise from the rod and the airfoil. The

interference effects are always more pronounced in simulations and analytical solutions due to idealization of geometry and flow; small variations/asymmetries in experiments tend to "wash out" interference patterns. Also, such interference effects are not expected in the computation using Amiet's approach where only the noise from the airfoil is included.

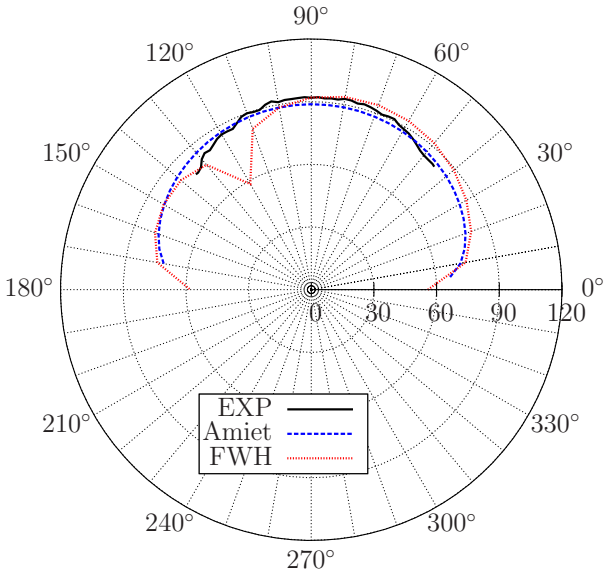

Figure 3.24: Directivity of the peak acoustic pressure (PSD at $St = 0.19$). The polar angle (values listed on the periphery of the plot) is measured from downstream.

Conclusions

A compressible (Charles) and an incompressible (pimpleFoam) LES solvers are used to analyze aerodynamic interaction between a rod and an airfoil in a tandem arrangement. The noise produced due to this interaction is analyzed using the Ffowcs Williams-Hawkings acoustic analogy with the compressible simulation and Amiet's formula with the incompressible simulation. The incompressible solver pimpleFoam coupled with Amiet's theory is benchmarked as a new methodology for noise prediction and validated against the rod-airfoil case. The predicted mean and r.m.s. velocity profiles and surface pressure, near-field velocity spectra, and far-field acoustic pressure spectra and directivity are compared with measurements. The following is concluded from the analyses.

1. The predictions of mean surface pressure on the rod surface are in good agreement with experiments, with the pimpleFoam results matching the data better. RMS pressure is overpredicted by both solvers with the pimpleFoam results showing a better agreement.

2. Mean flow comparisons show good agreement between the solvers but the agreement with the measured data is moderate. Velocity deficit and turbulence intensity in the wakes are generally over-predicted by the solvers. The over-prediction of turbulence intensity is higher in Charles.

3. The predictions of velocity PSDs in the near-field match well with the data in terms of capturing the peak frequencies and magnitude, as well as the spectral fall-off observed in the measured spectra. Integrated sectional lift and drag spectra show that peaks in the spectra exist at the fundamental wake shedding frequency ($St \sim 0.19$) for lift and at the first harmonic ($St \sim 0.38$) for drag. This is due to the symmetry in drag contribution from the alternate vortex shedding from the top and bottom halves of the cylinder, while the contribution to lift is asymmetric.

4. Spatial coherence, evaluated at the maximum airfoil thickness axial location shows that the coherence drops below 0.5 for $St > 0.38$ over a spanwise distance of $0.15c$, implying that for these frequencies, the choice of the span length of $0.33c$ is reasonable.

5. Far-field PSD comparisons with data are made by using Kato's correction for the differences in the span lengths. Good agreement with data is observed for both methods in the range $0.1 < St < 1$. The directivity comparison at the peak Strouhal number shows reasonable agreement with the data.

Acknowledgments

Funding for this research was provided by the General Electric Global Research Center and the Iowa Space Grants Consortium (Grant #475-20-5). Computational resources used for this research were provided by NSF XSEDE (Grant #TG-CTS130004) and by the Brookhaven National Laboratory.

CHAPTER 4. GENERAL CONCLUSIONS

The importance of broadband noise for overall aircraft noise is highlighted. Broadband noise production in an aircraft engine fan stage is not yet completely understood. It requires further investigation in order to explain a few of the noise scalings observed in wind tunnel experiments. The broadband noise production mechanisms are grouped into: (1) interaction, and (2) self noise sources, depending on the location of the origin of the turbulence which produces the noise. Fan broadband noise is dominated by rotor-stator interaction noise, which could be further understood by explaining the following noise scalings observed in experiments:

1. **Speed scaling:** The noise scales with M^3 instead of M^5 as predicted by theory.
2. **Vane count scaling:** The noise scales with the number of vanes in the OGV though only in high frequencies.
3. **Effect of vane sweep:** The noise scales with the sweep in the blades of the OGV.

For the validation case of aerodynamic interaction between a rod and an airfoil in a tandem arrangement, a compressible (Charles) and an incompressible (pimpleFoam) LES solvers are utilized. The farfield noise is predicted using the Ffowcs Williams-Hawkings acoustic analogy with the compressible simulation and Amiets theory with the incompressible simulation. Both methods gives good predictions for the noise with the correct decay for broadband noise and correct frequencies and amplitudes for tonal noise. The incompressible solver pimpleFoam coupled with Amiets theory is benchmarked as a new methodology for noise prediction and validated.

Bibliography

[1] R.E. Owens. Energy efficient engine: Propulsion system-aircraft integration evaluation. Technical report, 1979.

[2] P.J. Joseph and M.G. Smith. Aircraft noise. In Frank Fahy and John Walker, editors, *Advanced applications in acoustics, noise and vibration*, pages 292–346. CRC Press, London, 2004.

[3] U.W. Ganz, P.D. Joppa, T.J. Patten, and D.F. Scharpf. Boeing 18-inch fan rig broadband noise test. 1998.

[4] R.P. Woodward, C.E. Hughes, R.J. Jeracki, and C.J. Miller. Fan noise source diagnostic testfar-field acoustic results. *AIAA paper*, 2427, 2002.

[5] C. Cheong, P. Joseph, and S. Lee. High frequency formulation for the acoustic power spectrum due to cascade-turbulence interaction. *The Journal of the Acoustical Society of America*, 119(1):108–122, 2006.

[6] W.R. Sears. Some aspects of non-stationary airfoil theory and its practical application. *Journal of the Aeronautical Sciences*, 8(3):104–188, 1941.

[7] C. Norberg. Pressure forces on a circular cylinder in cross flow. In *Bluff-Body Wakes, Dynamics and Instabilities*, pages 275–278. Springer, 1993.

[8] E. Envia. Emerging community noise reduction approaches. 2011.

[9] B. Callender, E.J. Gutmark, and S. Martens. Far-field acoustic investigation into chevron nozzle mechanisms and trends. *AIAA journal*, 43(1):87–95, 2005.

[10] J.M. Tyler and T.G. Sofrin. Axial flow compressor noise studies. Technical report, SAE Technical Paper, 1962.

[11] P.R. Gliebe. Fan broadband noise-the floor to high bypass engine noise reduction. In *Noise Con*, pages 133–138, 1996.

[12] J.E. Ffowcs Williams and D.L. Hawkings. Theory relating to the noise of rotating machinery. *Journal of Sound and Vibration*, 10(1):10–21, 1969.

[13] C.E. Hughes, R. Jeracki, R. Woodward, and C. Miller. Fan noise source diagnostic testrotor alone aerodynamic performance results. In *8th AIAA/CEAS Aeroacoustics Conference, Breckenridge, CO, June*, pages 17–19, 2002.

[14] G.G. Podboy and S.M. Helland. Fan noise source diagnostic test-two-point hot-wire results. *AIAA paper*, 2431, 2002.

[15] J. Premo. Fan noise source diagnostic test-circumferential mode measurements. *AIAA Paper*, 2429, 2002.

[16] L.J. Heidelberg. Fan noise source diagnostic testtone modal structure results. *NASA TM Paper*, (2002-211594), 2002.

[17] E. Envia. Fan noise source diagnostic test-vane unsteady pressure results. *AIAA Paper*, 2430:2002, 2002.

[18] M.J. Lighthill. On sound generated aerodynamically. i. general theory. *Proceedings of the Royal Society of London. Series A. Mathematical and Physical Sciences*, 211(1107): 564–587, 1952.

[19] M.J. Lighthill. On sound generated aerodynamically. ii. turbulence as a source of sound. In *Proceedings of the Royal Society of London A: Mathematical, Physical and Engineering Sciences*, volume 222, pages 1–32. The Royal Society, 1954.

[20] N. Curle. The influence of solid boundaries upon aerodynamic sound. *Proceedings of the Royal Society of London. Series A. Mathematical and Physical Sciences*, 231(1187): 505–514, 1955.

[21] J.E. Ffowcs Williams and D.L. Hawkings. Sound generation by turbulence and surfaces in arbitrary motion. *Philosophical Transactions of the Royal Society of London. Series A, Mathematical and Physical Sciences*, 264(1151):321–342, 1969.

[22] T.F. Brooks, D.S. Pope, and M.A. Marcolini. *Airfoil self-noise and prediction*, volume 1218. National Aeronautics and Space Administration, Office of Management, Scientific and Technical Information Division, 1989.

[23] J.E. Ffowcs Williams and L.H. Hall. Aerodynamic sound generation by turbulent flow in the vicinity of a scattering half plane. *Journal of Fluid Mechanics*, 40(04):657–670, 1970.

[24] M.S. Howe. A review of the theory of trailing edge noise. *Journal of Sound and Vibration*, 61(3):437–465, 1978.

[25] R.K. Amiet. Noise due to turbulent flow past a trailing edge. *Journal of Sound and Vibration*, 47(3):387–393, 1976.

[26] J. Casper and F. Farassat. Broadband trailing edge noise predictions in the time domain. *Journal of Sound and Vibration*, 271(1):159–176, 2004.

[27] M. Roger and S. Moreau. Broadband self noise from loaded fan blades. *AIAA journal*, 42 (3):536–544, 2004.

[28] I.F. Cozza, A. Iob, and R. Arina. Broadband trailing-edge noise prediction with a stochastic source model. *Computers & Fluids*, 57:98–109, 2012.

[29] A. Finez, E. Jondeau, M. Roger, and M.C. Jacob. Broadband noise reduction with trailing edge brushes. In *16th AIAA/CEAS Aeroacoustics Conference*, 2010.

[30] T.P. Chong, P.F. Joseph, and M. Gruber. Airfoil self noise reduction by non-flat plate type trailing edge serrations. *Applied Acoustics*, 74(4):607–613, 2013.

[31] M.E. Goldstein. Aeroacoustics. *New York, McGraw-Hill International Book Co., 1976. 305 p.*, 1, 1976.

[32] R.K. Amiet. Acoustic radiation from an airfoil in a turbulent stream. *Journal of Sound and vibration*, 41(4):407–420, 1975.

[33] C.B. Lorence and K.C. Hall. Sensitivity analysis of the aeroacoustic response of turbomachinery blade rows. *AIAA journal*, 34(8):1545–1554, 1996.

[34] I. Evers and N. Peake. On sound generation by the interaction between turbulence and a cascade of airfoils with non-uniform mean flow. *Journal of Fluid Mechanics*, 463:25–52, 2002.

[35] W.J. Devenport, J.K. Staubs, and S.A.L. Glegg. Sound radiation from real airfoils in turbulence. *Journal of Sound and Vibration*, 329(17):3470–3483, 2010.

[36] T. Von Kármán and W.R. Sears. Airfoil theory for non-uniform motion. *Journal of the Aeronautical Sciences*, 5(10):379–390, 1938.

[37] H. Kobayashi. Three-dimensional effects on pure tone fan noise due to inflow distortion. In *11th Fluid and Plasma Dynamics Conference*, volume 1, 1978.

[38] L.T. Filotas. Theory of airfoil response in a gusty atmosphere. part i. aerodynamic transfer function. Technical report, University of Toronto, 1969.

[39] J.M.R. Graham. Similarity rules for thin aerofoils in non-stationary subsonic flows. *Journal of Fluid Mechanics*, 43(04):753–766, 1970.

[40] J.J. Adamczyk and R.S. Brand. Scattering of sound by an aerofoil of finite span in a compressible stream. *Journal of Sound and Vibration*, 25(1):139–156, 1972.

[41] S.N. Smith. *Discrete frequency sound generation in axial flow turbomachines*. PhD thesis, Citeseer, 1971.

[42] D.S. Whitehead. *Vibration and sound generation in a cascade of flat plates in subsonic flow*. 1970.

[43] D.S. Whitehead. Classical two-dimensional methods. *In AGARD Aeroelasticity in Axial-Flow Turbomachines.*, 1, 1987.

[44] S.A.L. Glegg. The response of a swept blade row to a three-dimensional gust. *Journal of sound and vibration*, 227(1):29–64, 1999.

[45] A.J. Cooper and N. Peake. Rotor-stator interaction noise in swirling flow: Stator sweep and lean effects. *AIAA journal*, 44(5):981–991, 2006.

[46] Q. Zhou and P. Joseph. A frequency domain numerical method for airfoil broadband self-noise prediction. *Journal of sound and vibration*, 299(3):504–519, 2007.

[47] H. Posson, S. Moreau, and M. Roger. Broadband noise prediction of fan outlet guide vane using a cascade response function. *Journal of Sound and Vibration*, 330(25):6153–6183, 2011.

[48] V.V. Golubev and H.M. Atassi. Acoustic–vorticity waves in swirling flows. *Journal of Sound and Vibration*, 209(2):203–222, 1998.

[49] P. Joseph and C.L. Morfey. Multimode radiation from an unflanged, semi-infinite circular duct. *The Journal of the Acoustical Society of America*, 105(5):2590–2600, 1999.

[50] H. Levine and J. Schwinger. On the radiation of sound from an unflanged circular pipe. *Physical review*, 73(4):383, 1948.

[51] L.A. Weinstein. The theory of diffraction and the factorization method. 1969.

[52] E.J. Rice. Modal density function and number of propagating modes in ducts. *The Journal of the Acoustical Society of America*, 60(S1):S112–S112, 1976.

[53] S.A.L. Glegg. The tailored greens function for a forward facing step. *Journal of Sound and Vibration*, 332(17):4037–4044, 2013.

[54] M.C. Jacob, J. Boudet, D. Casalino, and M. Michard. A rod-airfoil experiment as a benchmark for broadband noise modeling. *Theoretical and Computational Fluid Dynamics*, 19(3):171–196, 2005.

[55] D. Casalino, M. Jacob, and M. Roger. Prediction of rod-airfoil interaction noise using the ffowcs-williams-hawkings analogy. *AIAA journal*, 41(2):182–191, 2003.

[56] J. Boudet, N Grosjean, and M.C. Jacob. Wake-airfoil interaction as broadband noise source: a large-eddy simulation study. *International Journal of Aeroacoustics*, 4(1):93–116, 2005.

[57] J. Berland, P. Lafon, F. Crouzet, F. Daude, and C. Bailly. Numerical insight into sound sources of a rod-airfoil flow configuration using direct noise calculation. In *16th AIAA/CEAS Aeroacoustics Conference*, 2010.

[58] A. Eltaweel and M. Wang. Numerical simulation of broadband noise from airfoil-wake interaction. *AIAA Paper*, 2802:5–8, 2011.

[59] J.C. Giret, A. Sengissen, S. Moreau, M. Sanjosé, and J.C. Jouhaud. Prediction of the sound generated by a rod-airfoil configuration using a compressible unstructured les solver and a fw-h analogy. *AIAA Paper*, 2058:4–6, 2012.

[60] J.C. Giret, A. Sengissen, S. Moreau, M. Sanjosé, and J.C. Jouhaud. Noise source analysis of a rod-airfoil configuration using unstructured large-eddy simulation. *AIAA Journal*, pages 1–16, Aug 2014. ISSN 0001-1452. doi: 10.2514/1.J053371. URL http://dx.doi.org/10.2514/1.J053371.

[61] A.W. Vreman. An eddy-viscosity subgrid-scale model for turbulent shear flow: Algebraic theory and applications. *Physics of Fluids (1994-present)*, 16(10):3670–3681, 2004.

[62] J. Smagorinsky. General circulation experiments with the primitive equations: I. the basic experiment*. *Monthly weather review*, 91(3):99–164, 1963.

[63] R.I. Issa. Solution of the implicitly discretised fluid flow equations by operator-splitting. *Journal of computational physics*, 62(1):40–65, 1986.

[64] S.V. Patankar and D.B. Spalding. A calculation procedure for heat, mass and momentum transfer in three-dimensional parabolic flows. *International Journal of Heat and Mass Transfer*, 15(10):1787–1806, 1972.

[65] D.P. Lockard. A comparison of ffowcs williams-hawkings solvers for airframe noise applications. *AIAA paper*, 2580(8), 2002.

[66] M.L. Shur, P.R. Spalart, and M.K. Strelets. Noise prediction for increasingly complex jets. part i: Methods and tests. *International Journal of Aeroacoustics*, 4(3):213–246, 2005.

[67] C. Kato and M. Ikegawa. Large eddy simulation of unsteady turbulent wake of a circular cylinder using the finite element method. In *Advances in Numerical Simulation of Turbulent Flows*, volume 1, pages 49–56, 1991.

[68] E. Achenbach. Distribution of local pressure and skin friction around a circular cylinder in cross-flow up to re= 5× 106. *Journal of Fluid Mechanics*, 34(04):625–639, 1968.

APPENDIX A. TIME SERIES ANALYSIS

Cross-correlation between two random processes which are functions of time, say $u(t)$ and $v(t)$, is defined as

$$R_{uv}(\tau) = \lim_{T\to\infty} \frac{1}{T} \int_0^T u(t)v(t+\tau)\ \mathrm{d}t. \tag{A.1}$$

If the processes $u(t)$ and $v(t)$ correspond to time signals of a stochastic quantity (say pressure in a turbulent flow) measured at two different spatial locations $\mathbf{x}$ and $\mathbf{y}$, then the cross correlation between these two random processes is called the two-point cross correlation function of that quantity (pressure) and expressed as

$$R_{xy}(\tau) = \lim_{T\to\infty} \frac{1}{T} \int_0^T p(\mathbf{x},t)p(\mathbf{y},t+\tau)\ \mathrm{d}t. \tag{A.2}$$

Cross-spectral density or cross power spectrum is defined as the Fourier transform of $R_{xy}(\tau)$ as

$$S_{xy}(\omega) = \int_{-\infty}^{\infty} R_{xy}(\tau)\ \exp(-i\omega\tau)\ \mathrm{d}\tau. \tag{A.3}$$

If the two points $\mathbf{x}$ and $\mathbf{y}$ are identical, then the cross-correlation reduces to autocorrelation, denoted by $R_{pp}(\tau)$, and the cross-spectral density reduces to power spectral density (PSD). These are defined as

$$R_{pp}(\tau) = \lim_{T\to\infty} \frac{1}{T} \int_0^T p(t)p(t+\tau)\ \mathrm{d}t \text{ and}$$

$$S_{pp}(\omega) = \int_{-\infty}^{\infty} R_{pp}(\tau)\ \exp(-i\omega\tau)\ \mathrm{d}\tau. \tag{A.4}$$

The Wiener-Khinchin theorem as can be used to compute PSD as

$$S_{pp}(\omega) = E|\hat{p}(\omega)|^2 \tag{A.5}$$
$$= \frac{1}{T}\int_0^T p^*(t)\exp(i\omega t)\,\mathrm{d}t \int_0^T p(t')\exp(-i\omega t')\,\mathrm{d}t',$$

where $\hat{p}(\omega)$ is the Fourier transform of $p(t)$. PSD for a discrete series (p_n) with N points, can be obtained using

$$S_{pp}(\omega) = \frac{(\delta t)^2}{T}\Big|\sum_{n=1}^{N} p_n \exp(-i\omega\ n\delta t)\Big|^2. \tag{A.6}$$

PSD calculations are typically averaged over multiple samples to reduce the statistical scatter in the spectra.

Spatial coherence between two points $\mathbf{x}$ and $\mathbf{y}$ is defined as

$$\gamma_{xy}^2(\omega) = \frac{|S_{xy}(\omega)|^2}{S_{xx}(\omega)S_{yy}(\omega)}, \tag{A.7}$$

where $S_{xx}(\omega)$ is $S_{pp}(\omega)$ evaluated at $\mathbf{x}$ and $S_{yy}(\omega)$ is $S_{pp}(\omega)$ evaluated at $\mathbf{y}$.

ACKNOWLEDGMENTS

I would first like to acknowledge the guidance and motivation from my major professor, Dr. Anupam Sharma. This work would not be possible without his support.

I would also like to acknowledge Dr. Alric Rothmayer, Dr. Alberto Passalacqua, Dr. Jue Yan (MATH), Karthik Rudra Reddy and my research group for some fruitful discussions.